Dynamic Stability Analysis and Improved LVRT Schemes of DFIG-Based Wind Turbines During a Symmetrical Fault in a Weak Grid

Ruikuo Liu, Jun Yao, *Member, IEEE*, Xuewei Wang, Peng Sun, Jinxin Pei, and Jiabing Hu, *Senior Member, IEEE*

***Abstract*—With the increasing penetration of the wind power, the stability issues of the weak AC grid-connected doubly fed induction generator (DFIG)-based wind turbines during low-voltage ride through (LVRT) cannot be neglected. In order to explore the instability mechanism of DFIG system during weak grid fault, the small signal state-space model is established in this paper. The results of the modal analysis show that the dominant unstable poles are mainly impacted by the phase-locked loop (PLL), rotor current control loop, and terminal voltage during the fault, where the PLL is the dominant factor. Furthermore, the impact of each factor on the system dynamic stability is comprehensively evaluated, which indicates that the controller bandwidth under normal grid condition is no longer applicable to the fault condition due to the interaction between the controller and grid. Then, the optimal current proportion which can significantly improve the system stability is deduced. Finally, based on the analysis, this paper proposes the improved LVRT control schemes from two aspects of either injecting active current or decreasing PLL bandwidth to enhance the small signal stability of the system. The effectiveness of the proposed LVRT control strategies is validated by the simulation and experiments.**

***Index Terms*—Doubly fed induction generator (DFIG), improved control schemes, low-voltage ride through (LVRT), phase-locked loop (PLL), rotor current control loop (RCCL), small signal stability, weak grid.**

NOMENCLATURE

$\boldsymbol{U}, \boldsymbol{I}, \boldsymbol{\Psi}$	Voltage, current, and flux linkage vectors.
$\omega_{\mathrm{g}}, \omega_{\mathrm{r}}$	Synchronous and rotor angular frequency.
$R_{\mathrm{s}}, R_{\mathrm{r}}$	Stator and rotor resistances of DFIG.
$L_{\mathrm{s}}, L_{\mathrm{r}}, L_{\mathrm{m}}$	Stator, rotor, and mutual inductances of DFIG.
$R_{\mathrm{L}}, L_{\mathrm{L}}$	Equivalent resistance and inductance of the transmission lines.
C_{f}	Filter capacitor.
$\theta_{\mathrm{pll}}, \omega_{\mathrm{pll}}$	Output angle and angular frequency of PLL.

Subscripts

d, q	Dq-axis components in PLL reference frame.
s, r	Stator- and rotor-side quantities.
b, 0	Basic value and initial value.

Superscripts

$*$	Reference value.

Manuscript received November 15, 2018; revised March 13, 2019; accepted April 7, 2019. Date of publication April 14, 2019; date of current version October 18, 2019. This work was supported in part by the National Key Research and Development Program of China under Grant 2017YFB0902000 and in part by the 111 Project of China under Grant B18062. Recommended for publication by Associate Editor M. S. ElMoursi. *(Corresponding author: Jun Yao.)*

R. Liu, J. Yao, X. Wang, P. Sun, and J. Pei are with the State Key Laboratory of Power Transmission Equipment & System Security and New Technology, School of Electrical Engineering, Chongqing University, Chongqing 400044, China (e-mail: liuruikuo1986@163.com; jyao@cqu.edu.cn; wangxueweihlg@163.com; wdfasfe@qq.com; peijinxindoc@163.com).

J. Hu is with the State Key Laboratory of Advanced Electromagnetic Engineering and Technology and the School of Electrical and Electronic Engineering, Huazhong University of Science and Technology, Wuhan 430074, China (e-mail: j.hu@mail.hust.edu.cn).

Color versions of one or more of the figures in this paper are available online at http://ieeexplore.ieee.org.

Digital Object Identifier 10.1109/TPEL.2019.2911346

I. INTRODUCTION

WITH the rapid development of the wind power industry, the wind power generation system has been widely installed in the world [1], [2]. Moreover, due to the distribution of the wind energy, the large-scale wind farms are usually located in the remote areas, which connect grid via long transmission lines with high impedance. Consequently, the short-circuit ratio (SCR) of the system is lower [3], [4]. When the far-end fault occurs in the weak grid, affected by the high impedance of the transmission line, there is a risk that the typical low-voltage ride through (LVRT) control strategy of the wind turbines may not work [5]. Especially, since the stator of the doubly fed induction generator (DFIG)-based wind turbine is directly coupled to the grid and the rating of the back-to-back converter is limited, the DFIG system is very sensitive to the grid fault [6], [7]. The dips of the voltage in the weak grid will bring undesirable dynamics to the controller of the DFIG-based wind turbines and may cause the small signal instability of the system [8], [9]. In addition, the small signal instability may further trigger the large signal instability issues when the system loses the equilibrium point. Therefore, the stability issues of the DFIG-based wind turbines under symmetrical faults in the weak grid should be further investigated.

Recently, some studies about the stability issues of the DFIG system have been carried out. In [10], the DFIG system impedance considering the phase-locked loop (PLL) is established and it is indicated that the PLL with fast control dynamics may result in the occurrence of the middle frequency resonance.

Wang *et al.* [11] analyzed the relationship between the PI parameters of the PLL and the low-frequency oscillation of the DFIG system. Xi *et al.* [12] proposed an enhanced model of the DFIG-based wind farm and analyzed the influence of the PLL and the rotor current control loop (RCCL) on the small signal stability of the weak power system involving the DFIG-based wind turbines. In [13], the small signal behavior of the DFIG system is studied under DC-link voltage timescale and the dynamics of the current controller is omitted. However, the above researches on stability issues are based on the condition of the normal power grid voltage, which cannot explain the dynamic instability mechanism of the DFIG system under large disturbance. In [14], the improved PLL structure is proposed to enhance the LVRT capability of the DFIG system, but the relationship between the PLL and the dynamic stability of the system under weak grid fault is not involved. Ye *et al.* [15] and Alsmadi *et al.* [16] study the influence of the rotor dynamic and the different fault types on the small signal behavior of the DFIG system, respectively, but due to the omitting of the dynamic of the PLL and the grid resistance, the analysis results of the influence on the dynamic stability of the DFIG system during LVRT may not be accurate. In [17], the impacts of controller bandwidth and active current reference on the dynamic stability of the DFIG system under the far-end severe fault of the weak grid are analyzed by using the method of the complex phase coefficients. Liu *et al.* [18] analyzed the influence of the voltage dips degree and controller bandwidth on the dynamic stability of the DFIG system by adopting the state-space equation-based eigenvalue analysis method. However, the influence of the fault position on the small signal stability is not researched in [17], [18] and there is no effective oscillation suppression strategy proposed. Moreover, in [17], the grid fault is simulated by injecting disturbance in PLL, which is not a real voltage sag. Therefore, the results of the paper cannot truly reflect the oscillation modality of the system during weak grid fault and explore the influence of the voltage dips degree, control parameters, and other factors on the dynamic stability of the DFIG system.

From the above, the small signal stability of the DFIG system under the weak grid fault has not been fully investigated. To fill in the gaps in existing literature and solve the aforementioned problems, this paper established the small signal state-space equation to more comprehensively evaluate the dynamic instability risk of the DFIG system during symmetrical fault in a weak grid. Based on the evaluation results, there are two main contributions in this paper as follows: (1) According to the small signal state-space equation and the vector relationship between terminal voltage and grid voltage, this paper points out from the mechanism that the damping ratio of the dominant poles for the DFIG system can be significantly improved by injecting reasonable active current into the grid during the fault. Based on this, a novel optimal active and reactive current proportion scheme is proposed, which can minimize the instability risk of the system during LVRT while meeting the requirements of the grid code. (2) Based on the eigenvalues locus analysis, a PLL bandwidth selection method during grid fault is proposed, which takes into account the controllers' interaction and can effectively improve the dynamic stability of the system without changing the control structure.

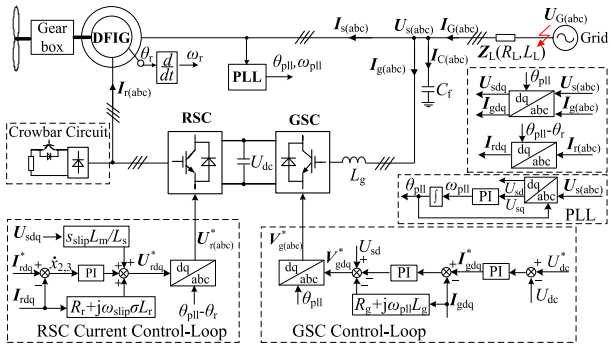

Fig. 1. Block diagram of DFIG-based wind turbine during LVRT.

The correctness of the theoretical analysis and the effectiveness of the proposed two control strategies are validated by the time-domain simulation and the laboratory-scale DFIG rig. The paper is organized as follows. In Section II, the detailed small signal state-space model is established. In Section III, the influence of the dominant factors on the small signal stability of the DFIG system is investigated. In Section IV, the improved LVRT control schemes are proposed. Section V presents the simulation and experimental results. Finally, the conclusion is drawn in Section VI.

II. Small Signal State-Space Model

The configuration diagram and typical LVRT strategy of the DFIG-based wind turbine under grid faults are shown in Fig. 1. Based on the Thevenin theorem, the power grid is equivalent to a voltage source $\boldsymbol{U}_{\mathrm{G}}$ and impedance $\boldsymbol{Z}_{\mathrm{L}}$ in series. $\boldsymbol{Z}_{\mathrm{L}}$ is composed of the transmission line impedance and step-up transformers impedance between the fault point and terminal of the DFIG-based wind turbines.

According to the grid code [19], the DFIG-based wind turbines are required to inject reactive current in proportion to the voltage dips degree during the fault. However, under the weak grid, due to the increased coupling between the power grid and the controller of the wind turbines, the traditional LVRT strategy may cause the small signal instability of the system, which is omitted by the grid code. In order to investigate the stability issues of the weak grid-connected DFIG system during LVRT, a detailed small signal state-space model needs to be established.

A. DFIG Model

According to the motor convention, the per unit voltage and flux equations of DFIG in the PLL reference frame can be written as [20]

$$\begin{cases} \boldsymbol{U}_{\mathrm{sdq}} = R_{\mathrm{s}}\boldsymbol{I}_{\mathrm{sdq}} + \dot{\boldsymbol{\Psi}}_{\mathrm{sdq}}/\omega_{\mathrm{b}} + \mathrm{j}\omega_{\mathrm{pll}}\boldsymbol{\psi}_{\mathrm{sdq}} \\ \boldsymbol{U}_{\mathrm{rdq}} = R_{\mathrm{r}}\boldsymbol{I}_{\mathrm{rdq}} + \dot{\boldsymbol{\Psi}}_{\mathrm{rdq}}/\omega_{\mathrm{b}} + \mathrm{j}(\omega_{\mathrm{pll}} - \omega_{\mathrm{r}})\boldsymbol{\psi}_{\mathrm{rdq}} \end{cases} \tag{1}$$

$$\begin{cases} \boldsymbol{\psi}_{\mathrm{sdq}} = L_{\mathrm{s}}\boldsymbol{I}_{\mathrm{sdq}} + L_{\mathrm{m}}\boldsymbol{I}_{\mathrm{rdq}} \\ \boldsymbol{\psi}_{\mathrm{rdq}} = L_{\mathrm{r}}\boldsymbol{I}_{\mathrm{rdq}} + L_{\mathrm{m}}\boldsymbol{I}_{\mathrm{sdq}}. \end{cases} \tag{2}$$

Based on (1) and (2), the dynamics of the DFIG can be expressed as

$$\dot{\boldsymbol{I}}_{\mathrm{sdq}} = \left[-\frac{\omega_{\mathrm{b}}R_{\mathrm{s}}}{\sigma L_{\mathrm{s}}} - \mathrm{j}\omega_{\mathrm{b}}\left(\omega_{\mathrm{pll}} + \frac{L_{\mathrm{m}}^2}{\sigma L_{\mathrm{r}}L_{\mathrm{s}}}\omega_{\mathrm{r}}\right)\right]\boldsymbol{I}_{\mathrm{sdq}} + \left(\frac{\omega_{\mathrm{b}}L_{\mathrm{m}}R_{\mathrm{r}}}{\sigma L_{\mathrm{s}}L_{\mathrm{r}}} - \mathrm{j}\frac{\omega_{\mathrm{b}}L_{\mathrm{m}}}{\sigma L_{\mathrm{s}}}\omega_{\mathrm{r}}\right)\boldsymbol{I}_{\mathrm{rdq}} + \frac{\omega_{\mathrm{b}}}{\sigma L_{\mathrm{s}}}\boldsymbol{U}_{\mathrm{sdq}} - \frac{\omega_{\mathrm{b}}L_{\mathrm{m}}}{\sigma L_{\mathrm{s}}L_{\mathrm{r}}}\boldsymbol{U}_{\mathrm{rdq}} \tag{3a}$$

$$\dot{\boldsymbol{I}}_{\mathrm{rdq}} = \left(\frac{\omega_{\mathrm{b}}L_{\mathrm{m}}R_{\mathrm{s}}}{\sigma L_{\mathrm{s}}L_{\mathrm{r}}} + \mathrm{j}\frac{\omega_{\mathrm{b}}L_{\mathrm{m}}}{\sigma L_{\mathrm{r}}}\omega_{\mathrm{r}}\right)\boldsymbol{I}_{\mathrm{sdq}} - \left[\frac{\omega_{\mathrm{b}}R_{\mathrm{r}}}{\sigma L_{\mathrm{r}}} + \mathrm{j}\omega_{\mathrm{b}}\left(\omega_{\mathrm{pll}} - \frac{\omega_{\mathrm{r}}}{\sigma}\right)\right]\boldsymbol{I}_{\mathrm{rdq}} - \frac{\omega_{\mathrm{b}}L_{\mathrm{m}}}{\sigma L_{\mathrm{s}}L_{\mathrm{r}}}\boldsymbol{U}_{\mathrm{sdq}} + \frac{\omega_{\mathrm{b}}}{\sigma L_{\mathrm{r}}}\boldsymbol{U}_{\mathrm{rdq}} \tag{3b}$$

where $\sigma = 1 - L_{\mathrm{m}}^2/(L_{\mathrm{s}}L_{\mathrm{r}})$.

B. PLL Model

The PLL is an automatic closed-loop control system that can synchronize the dq frame of controller with the AC grid. The typical PLL is shown in Fig. 1, which can be depicted as

$$\begin{cases} \dot{x}_1 = U_{\mathrm{sq}} \\ \omega_{\mathrm{pll}} = k_{\mathrm{p1}}U_{\mathrm{sq}} + k_{\mathrm{i1}}x_1 \\ \dot{\theta}_{\mathrm{pll}} = \omega_{\mathrm{b}}\omega_{\mathrm{pll}} \end{cases} \tag{4}$$

where k_{p1} and k_{i1} are proportional coefficient and integration coefficient of the PLL's PI controller, respectively.

C. RCCL Model

During LVRT, the rotor-side converter (RSC) of DFIG-based wind turbine is controlled to inject reactive current into the power grid according to the grid code and the remaining current capacity of RSC can be used to output active current to alleviate mechanical stress [21], as shown in Fig. 1. Adopting the stator voltage orientation, the RCCL can be described as

$$\begin{cases} \dot{x}_2 = I_{\mathrm{rd}}^* - I_{\mathrm{rd}} \\ U_{\mathrm{rd}} = k_{\mathrm{p2}}\dot{x}_2 + k_{\mathrm{i2}}x_2 + \frac{(\omega_{\mathrm{pll}}-\omega_{\mathrm{r}})L_{\mathrm{m}}}{L_{\mathrm{s}}}U_{\mathrm{sd}} \\ \qquad -(\omega_{\mathrm{pll}} - \omega_{\mathrm{r}})\sigma L_{\mathrm{r}}I_{\mathrm{rq}} + R_{\mathrm{r}}I_{\mathrm{rd}} \\ \dot{x}_3 = I_{\mathrm{rq}}^* - I_{\mathrm{rq}} \\ U_{\mathrm{rq}} = k_{\mathrm{p3}}\dot{x}_3 + k_{\mathrm{i3}}x_3 + (\omega_{\mathrm{pll}} - \omega_{\mathrm{r}})\sigma L_{\mathrm{r}}I_{\mathrm{rd}} + R_{\mathrm{r}}I_{\mathrm{rq}} \end{cases} \tag{5}$$

where k_{p2} and k_{i2} are the parameters of the d-axis current control loop's PI controller, respectively; k_{p3} and k_{i3} are the parameters of the q-axis current control loop's PI controller, respectively.

D. Power Grid Model

Generally, the task of injecting reactive current is undertaken by the RSC, and GSC is only responsible for maintaining the DC-link voltage and dealing with the slip power. Moreover, the modal analysis in [18] and [22] also indicates that the GSC controller rarely affects the system stability. The dynamics of a given GSC are actually conducted by the RSC which plays a fundamental role in the dynamic behavior of DFIG system. Therefore, in order to reduce the dimension of the small signal state-space equation and simplify the analysis, the GSC's impact is omitted in the following analysis.

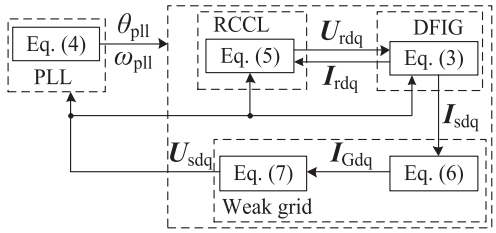

Fig. 2. Coupling relationship of DFIG system under the weak grid fault.

Based on the above explanation, the per unit line current in the PLL reference frame can be simplified as

$$\boldsymbol{I}_{\mathrm{Gdq}} = \boldsymbol{I}_{\mathrm{sdq}} + C_{\mathrm{f}}\dot{\boldsymbol{U}}_{\mathrm{sdq}}/\omega_{\mathrm{b}} + \mathrm{j}\omega_{\mathrm{pll}}C_{\mathrm{f}}\boldsymbol{U}_{\mathrm{sdq}} \tag{6}$$

According to Fig. 1, the relationship between the terminal voltage and grid voltage in the PLL reference frame can be described as

$$\boldsymbol{U}_{\mathrm{sdq}} = \boldsymbol{U}_{\mathrm{Gdq}} - (R_{\mathrm{L}} + \mathrm{j}\omega_{\mathrm{pll}}L_{\mathrm{L}})\boldsymbol{I}_{\mathrm{Gdq}} - L_{\mathrm{L}}\dot{\boldsymbol{I}}_{\mathrm{Gdq}}/\omega_{\mathrm{b}} \tag{7}$$

Based on (3)–(7), the coupling relationship of the DFIG system during the weak grid faults can be represented in Fig. 2. It can be seen that due to the high impedance of the lines, the undesirable dynamics of the controller caused by the dips of the grid voltage will seriously affect the terminal voltage of the DFIG-based wind turbine according to the transitive relation, which will affect the controller of the system again. The interaction may deteriorate the small signal stability of the DFIG system during LVRT.

To carry out the analysis of the dynamic stability of the DFIG system, the small signal state-space model should be obtained first. Linearizing (3)–(7) at steady-state operating point, the small signal state-space model during the weak grid fault can be expressed as

$$\begin{cases} \Delta\dot{\boldsymbol{x}} = \boldsymbol{A}\Delta\boldsymbol{x} + \boldsymbol{B}\Delta\boldsymbol{u} \\ 0 = \boldsymbol{C}\Delta\boldsymbol{x} + \boldsymbol{D}\Delta\boldsymbol{u} \end{cases} \tag{8}$$

where $\Delta\mathbf{x}$ is the state variable; $\Delta\boldsymbol{u}$ is the control variable; $\Delta\boldsymbol{x} = [\Delta I_{\mathrm{sd}}, \Delta I_{\mathrm{sq}}, \Delta I_{\mathrm{rd}}, \Delta I_{\mathrm{rq}}, \Delta x_2, \Delta x_3, \Delta I_{\mathrm{Gd}}, \Delta I_{\mathrm{Gq}}, \Delta U_{\mathrm{sd}}, \Delta U_{\mathrm{sq}}, \Delta x_1, \Delta\theta_{\mathrm{pll}}]^T$; $\Delta\boldsymbol{u} = [\Delta U_{\mathrm{rd}}, \Delta U_{\mathrm{rq}}, \Delta\omega_{\mathrm{pll}}]^T$. The detailed derivation of the small signal state-space model is given in Appendix A1. The small signal stability of the investigated DFIG system will be explored further in Section III.

III. Stability Analysis of DFIG System During LVRT

From (8), the small signal state-space model of DFIG system is a twelve-order model which has six oscillation modes. The oscillation modes will be changed greatly with the varying of

TABLE I
EIGENVALUES ANALYSIS RESULTS UNDER DIFFERENT VOLTAGE DIP DEGREES

U_G p.u.	Eigenvalue	Dominated state variables					Damping ratio
	$\lambda_{1,2}$	$\Delta\theta_{pll}$	ΔI_{rd}	ΔI_{rq}	ΔU_{sd}	ΔU_{sq}	$\xi_{1,2}$
0.3	-59±1205i	0.3602	0.1198	0.129	0.1977	0.1065	0.0492
0.25	5.6±1489i	0.3463	0.1132	0.1469	0.1845	0.1236	-0.00376
0.2	67.6±1551i	0.3314	0.1078	0.1665	0.1679	0.1417	-0.0435

voltage dips degree, fault position, controller parameters of the DFIG-based wind turbine, etc. The variation of the modes may result in the LVRT failure of the DFIG-based wind turbine. Thus, the influence of different factors on the small signal stability of the DFIG system during LVRT in the weak AC grid will be analyzed in this section. The circuit and controller parameters are given in Appendix A1. The SCR is normally used to evaluate the strength of the system. Generally, the smaller the SCR, the weaker the AC grid and the more unstable the system [23], [24]. Based on [23], a strong grid is known with the SCR higher than 3, and in a weak grid, the SCR would be between 2 and 3. The SCR is defined as [24]

$$\mathrm{SCR} = \frac{S_{\mathrm{PCC}}}{P_{\mathrm{rated}}} = \frac{U_{\mathrm{rated}}^2 / Z_{\mathrm{L}}}{P_{\mathrm{rated}}} \tag{9}$$

where the S_{PCC} is the short-circuit capacity at the point of common coupling (PCC), P_{rated} is the rated power of the DFIG, and U_{rated} is the AC-rated voltage. The S_{PCC} is about 7 kVA and P_{rated} is 3 kW of the investigated system. Therefore, based on (9), the SCR in this paper is about 2.3, which belongs to the weak grid.

To find out the dominant state variables that affect the unstable eigenvalues, the modal analysis is carried out. The participation factors of the dominant state variables and the damping ratio of the unstable eigenvalues are shown in Table I. It is indicated that the unstable eigenvalues are mainly impacted by the PLL, the RCCL, and the terminal voltage, where the PLL is the dominant factor. Combining with Fig. 2, the instability of DFIG system during the severe weak grid fault is essentially the oscillation instability caused by the interaction of the controllers under high transmission lines impedance. Additionally, it can also be seen from Table I that with the deepening of the voltage dips degree, the damping ratio of this oscillation mode is changed from positive to negative, which means that the system becomes unstable.

According to (6) and (7), the terminal voltage is closely related to the current of the DFIG system injected into the power grid and the transmission lines impedance. In other words, the terminal voltage is affected by the grid voltage dips degree and the fault position. Thus, the influence of voltage dips degree, the fault position, RCCL, and PLL on the small signal stability of the system will be analyzed as follows.

A. *Influence of the Voltage Dips Degree*

When the far-end fault occurs in the weak grid, as depicted in Fig. 1, the DFIG system injects the required reactive current according to the grid code [19]. Fig. 3 shows the eigenvalues varying with the voltage dips degree. It is observed that there

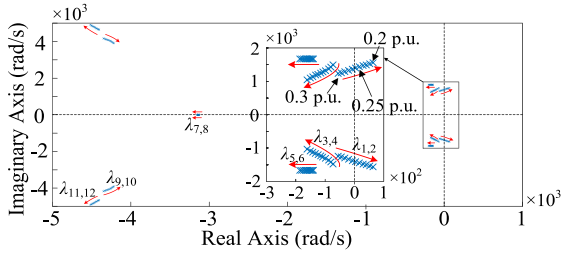

Fig. 3. Eigenvalues locus of the different voltage dips degree.

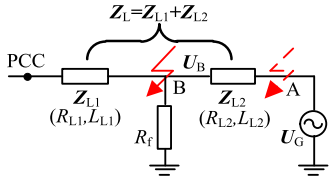

Fig. 4. Fault position schematic.

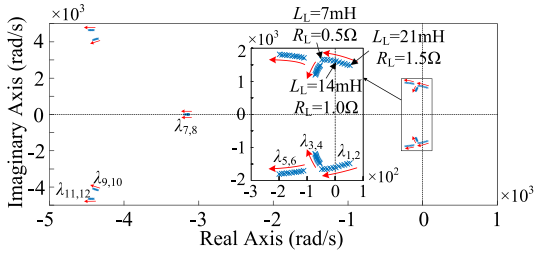

Fig. 5. Eigenvalues locus of different fault positions.

are a pair of eigenvalues moved to the right half-plane of s-plane under the severe grid fault, which indicates the small signal instability of the DFIG system and consistent with modal analysis. Without special statement, the severe grid fault refers to the fault point voltage dropping to 0.2 p.u.

B. *Influence of the Fault Position*

Assuming the fault position moves from point A to B, as shown in Fig. 4, then the short-circuit capacity at the PCC during severe grid fault can be expressed as

$$S = \frac{|\boldsymbol{U}_{\mathrm{B}}|^2}{\left|\boldsymbol{Z}_{\mathrm{L1}} + \frac{R_{\mathrm{f}}\boldsymbol{Z}_{\mathrm{L2}}}{R_{\mathrm{f}}+\boldsymbol{Z}_{\mathrm{L2}}}\right|} = \frac{|\boldsymbol{U}_{\mathrm{B}}|^2}{\left|\boldsymbol{Z}_{\mathrm{L1}} + \frac{R_{\mathrm{f}}}{R_{\mathrm{f}}/\boldsymbol{Z}_{\mathrm{L2}}+1}\right|} \tag{10}$$

where $\boldsymbol{U}_{\mathrm{B}}$ is the fault voltage of point B; R_{f} is the transition resistance.

It can be seen from (10), under the severe grid fault, when the fault position is close to the PCC, the short-circuit capacity at the PCC will increase, which means that the SCR is increased and the small signal stability of the DFIG system could be enhanced. Fig. 5 shows the eigenvalues locus of the different fault positions under the severe gird fault. The controller parameters are given in Appendix A1.

It can be seen that the dominant unstable poles move to the left half-plane as the fault position continues close to the PCC,

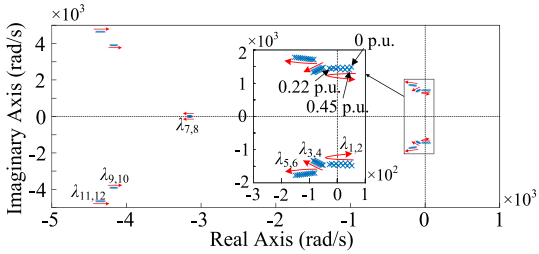

Fig. 6. Eigenvalues locus of the different active current references.

which also indicates that the small signal stability of the DFIG system is improved and consistent with analysis of (10).

Combining Figs. 3 and 5, it can be concluded that the farther the fault position away from PCC and the deeper the voltage dips degree, the easier the small signal instability of the DFIG system.

C. Influence of the RCCL Parameters

In this part, the influence of the active current reference and RCCL bandwidth on the system stability during LVRT will be investigated.

Generally, under the weak grid severe fault, the active current reference of RSC is set to zero. However, it was found in the experiments that the DFIG system injecting proper active current into the power grid during LVRT is beneficial to the small signal stability of system. Thus, in order to explain this phenomenon, the influence of the active current injection on the dominant unstable poles is further analyzed. Fig. 6 shows the eigenvalues locus of the different active current references of the RSC during the severe grid fault. The other parameters are the same with part A.

According to Fig. 6, with the increasing of the active current reference of the RSC, the dominant unstable poles move to the left and then move to the right. It is indicated that the DFIG-based wind turbine should inject active current into the grid for the small signal stability of the system. However, the active current reference has a certain range, which will be investigated as follows.

Assuming the voltage amplitude at the fault point will not change during the fault, the vector diagram of the terminal voltage and fault point voltage is given in Fig. 7.

During the weak grid fault, according to Fig. 7, q-axis voltage in PLL frame can be derived as

$$U_{\mathrm{sq}} = U_{\mathrm{G}} \sin\delta - I_{\mathrm{G}} Z_{\mathrm{L}} \sin(\theta_{\mathrm{I}} + \theta_{\mathrm{Z}}) \tag{11}$$

where θ_{I} and θ_{Z} are the phase angles of the power grid current and power grid impedance in the PLL reference frame, respectively. δ is the angle difference between the terminal voltage and fault point voltage.

Based on Fig. 7, (4) can be rewritten as

$$\begin{cases} \dot{x}_1 = U_{\mathrm{sq}} \\ \omega_{\mathrm{pll}} = k_{\mathrm{p1}} U_{\mathrm{sq}} + k_{\mathrm{i1}} x_1 \\ \dot{\delta} = \omega_{\mathrm{g}} - \omega_{\mathrm{pll}}. \end{cases} \tag{12}$$

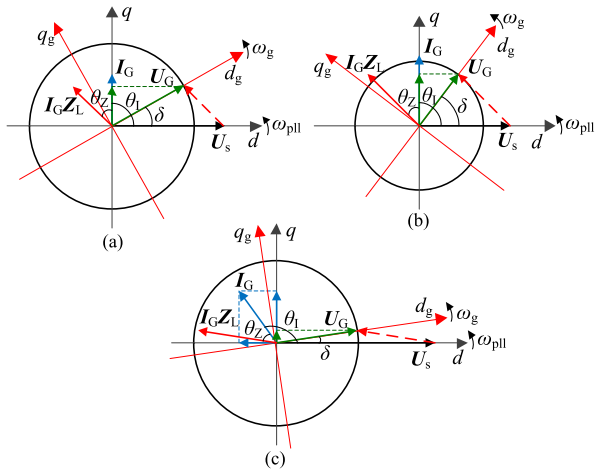

Fig. 7. Vector diagram of the terminal voltage and fault point voltage during grid fault. (a) and (b) The DFIG only output reactive current under different voltage dips degree. (c) The DFIG simultaneously output active and reactive current.

Assuming the feedback value of the current loop can follow the reference, when the fault location is determined, the second term of (11) can be regarded as constant. Therefore, combined with (11) and (12), the small signal state-space equations and characteristic function can be shown as (13) and (14), respectively.

$$\begin{bmatrix} \Delta\dot{x}_1 \\ \Delta\dot{\delta} \end{bmatrix} = \begin{bmatrix} 0 & U_{\mathrm{G}} \cos\delta_0 \\ -k_{\mathrm{i1}} & -k_{\mathrm{p1}} U_{\mathrm{G}} \cos\delta_0 \end{bmatrix} \begin{bmatrix} \Delta x_1 \\ \Delta\delta \end{bmatrix} = \boldsymbol{A}_1 \begin{bmatrix} \Delta x_1 \\ \Delta\delta \end{bmatrix} \tag{13}$$

$$|s\boldsymbol{I} - \boldsymbol{A}_1| = s^2 + s k_{\mathrm{p1}} U_{\mathrm{G}} \cos\delta_0 + k_{\mathrm{i1}} U_{\mathrm{G}} \cos\delta_0 = 0. \tag{14}$$

Equation (14) shows that when the $|\delta_0| < \pi/2$, the characteristic roots have negative real parts, which indicates the small signal stability in the DFIG system. According to (14), the damping ratio can be expressed as

$$\xi = \frac{k_{\mathrm{p1}} U_{\mathrm{G}} \cos\delta_0}{2\sqrt{k_{\mathrm{i1}} U_{\mathrm{G}} \cos\delta_0}} = \frac{k_{\mathrm{p1}}}{2} \sqrt{\frac{U_{\mathrm{G}} \cos\delta_0}{k_{\mathrm{i1}}}}. \tag{15}$$

It can be seen from (15) that the damping ratio reaches the maximum value when $\delta_0 = 0$. That is, during the grid fault, if δ is in the range of $[-\pi/2, \pi/2]$, the small signal stability of the system can be guaranteed, especially, when $\delta = 0$, the small signal stability of the system can be significantly improved, which is also consistent with the analysis in Fig. 6. In addition, it can be seen from (15) that as U_{G} decreases, the damping ratio decreases. Moreover, Fig. 7(a) and (b) also shows that with the deepening of the voltage dips degree, the DFIG system is required to increase the reactive current, leading to increase in δ and the instability risk of the system, which is consistent with Section III-A.

Therefore, in order to improve the stability of the system, it is necessary to reduce δ. Combined with Fig. 7(a) and (c), the DFIG system injecting active current into the power grid can decrease δ, which means that the PLL can easily trace the phase angle

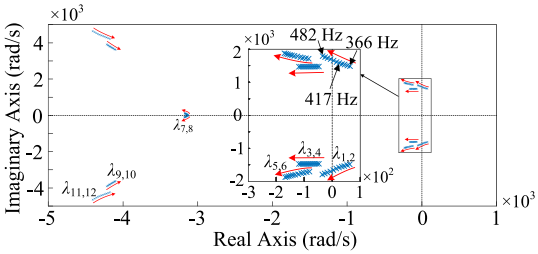

Fig. 8. Eigenvalues locus of different RCCL bandwidths.

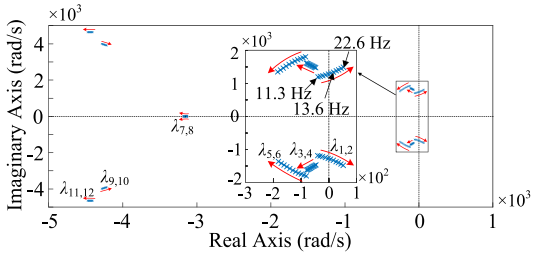

Fig. 9. Eigenvalues locus of different PLL's bandwidths.

of the grid voltage under such condition. As a consequence, the undesirable dynamics of the PLL caused by the terminal voltage dip might be reduced and the small signal stability of the system could be improved. Based on (11), when $\delta = 0$, the relationship between the dq-axis components of the grid current can be expressed as

$$I_{\mathrm{Gq}}/I_{\mathrm{Gd}} = -X_{\mathrm{L}}/R_{\mathrm{L}}. \tag{16}$$

Based on (2), (6), and (16), the optimal d-axis current reference of the RSC can be deduced as

$$I_{\mathrm{rd}}^{*} = \frac{L_{\mathrm{s}}R_{\mathrm{L}}}{L_{\mathrm{m}}X_{\mathrm{L}}}\left(\frac{\psi_{\mathrm{sq}} - L_{\mathrm{m}}I_{\mathrm{rq}}^{*}}{L_{\mathrm{s}}} + \frac{U_{\mathrm{sd}}}{X_{\mathrm{Cf}}}\right) \tag{17}$$

where Ψ_{sq} could be obtained by the flux observer. When the DFIG system injects the active current into the power grid according to (17), the small signal stability of the system will be significantly improved. In addition, it is worth noting that if the active current continues to increase, δ will enter the fourth quadrant and keep increasing, which may cause the system unstable again.

On the other hand, the bandwidth of the RCCL also influences the dominant unstable poles. Fig. 8 shows the eigenvalues locus with the varying of the RCCL bandwidth during the severe grid fault. As shown in Fig. 8, the dominant unstable poles move to the left half-plane of the s-plane with the increasing of the RCCL bandwidth from 366 to 482 Hz. It is indicated that the small signal stability of the DFIG system during LVRT can be enhanced by increasing the RCCL bandwidth.

D. Influence of the PLL Bandwidth

The typical block diagram of PLL can be seen in Fig. 1. Based on (4), the dynamic of the PLL directly impacts the phase angle δ. If the PLL bandwidth is inappropriate during the weak grid fault, small signal instability may occur in the DFIG system. In order to investigate the influence of the PLL bandwidth on the system stability during LVRT, $k_{\mathrm{p1}}/\sqrt{k_{\mathrm{i1}}}$ is assumed constant based on (15). Then, Fig. 9 shows the eigenvalues locus of the different PLL bandwidths during the severe grid fault. Other parameters are the same with part A.

As shown in Fig. 9, the dominant unstable poles move to the right half-plane of s-plane with the increasing of PLL bandwidth from 11.3 to 22.6 Hz. It is indicated that appropriately reducing the PLL bandwidth during LVRT is favorable to the small signal stability of the DFIG system. However, the dynamic response of the PLL will be deteriorated with decreasing of the bandwidth.

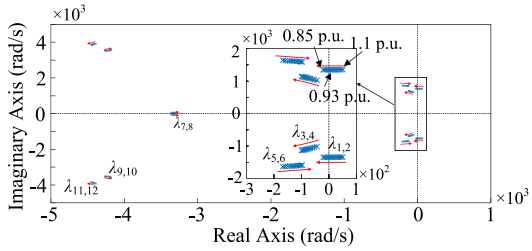

Fig. 10. Eigenvalues locus with different rotor speeds.

Therefore, under weak grid fault, the coordination between the small signal stability of system and the dynamic response of PLL should be noticed.

E. Influence of the Rotor Speed

According to the small signal state-space equations, the wind speed has influence on the initial state of the DFIG system at the power grid fault occurrence. Thus, the variation of the rotor speed may cause the dynamic instability of the DFIG system during LVRT. Due to the effect of the emergent pitch control and the large electromechanical time constant of the DFIG-based wind turbines, assuming the change of rotor speed is not sharp during gird fault and it is treated as constant [17].

In order to show the dominant poles passing through the imaginary axis when the rotor speed changes, the bandwidth of PLL is intentionally reduced to 15.6 Hz during the grid fault. Fig. 10 shows the eigenvalues locus with the varying of the rotor speed when the fault point voltage drops to 0.2 p.u. It can be seen from Fig. 10 that the dominant unstable poles move to the right half-plane of s-plane with the rotor speed increasing, which is indicated by the small signal instability of the DFIG system. That is, the weak grid fault that occurs at a higher rotor speed will bring higher risk for the dynamic stability of the DFIG system.

As a result, according to the above analysis, the mechanism of the small signal instability of the DFIG system can be summarized as that the interaction between the PLL and the RCCL during the weak grid fault causes the controller bandwidth under normal grid condition no longer applicable. The small signal stability of the DFIG system during LVRT can be improved by injecting appropriate active current, increasing the RCCL bandwidth or reducing the PLL bandwidth. It should be pointed out that the RCCL bandwidth is limited by the converter switching frequency. Hence, in practical applications, the method of

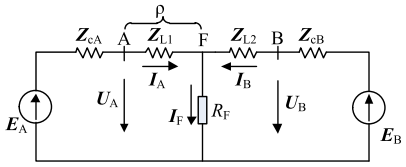

Fig. 11. Equivalent network of two terminal power supply.

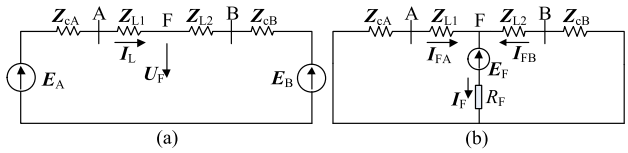

Fig. 12. (a) Pre-fault equivalent network. (b) Fault component equivalent network.

increasing the RCCL bandwidth to improve the small signal stability in the system during LVRT is not recommended.

IV. Improved Control Scheme During LVRT

The impact of the dominant factors on the small signal stability of the DFIG system has been investigated in Section III. In this section, the improved LVRT control schemes under the weak grid fault will be proposed from two aspects of either active current injection or decreasing PLL bandwidth.

A. Optimal Active and Reactive Current Proportion Scheme

When considering the impedance of the collecting power lines and step-up transformers, the $R_{\rm L}/X_{\rm L}$ of (17) is related to the fault position. That is, the determination of the fault position can provide a basis for the calculation of the active current reference. Thus, the fault location will be introduced in this paper. In [25] and [26], combining filtering and compensating, an improved single-terminal impedance fault location (IFL) algorithm was proposed. The maximum error of the algorithm is about 1% and the time of calculation is within milliseconds, which can meet the fault location requirements in this paper. Since fault location is not the focus of this paper, the algorithm proposed in [25] and [26] will be adopted directly in the proposed control strategy.

Now we use the equivalent network of two-terminal power supply to briefly introduce the calculation method of IFL. As shown in Fig. 11, the short-circuit fault occurs at point F where the distance from measurement point A is ρ. Fig. 12(a) and (b) shows the pre-fault equivalent network and the fault component equivalent network, respectively. When the parameters are linear, Fig. 11 can be regarded as the superposition of Fig. 12(a) and (b).

Based on Fig. 11, the impedance measured from A terminal can be written as

$$\boldsymbol{Z}_A = \boldsymbol{U}_A / \boldsymbol{I}_A = \boldsymbol{Z}_{\rm L1} + \boldsymbol{I}_F R_F / \boldsymbol{I}_A \tag{18}$$

where $\boldsymbol{U}_A$ and $\boldsymbol{I}_A$ are the voltage and current of measuring point A during fault, respectively; $Z_{\rm L1}$ is the line impedances from A to the fault point; $\boldsymbol{I}_{\rm F}$ is the fault component current flowing through transition resistance $R_{\rm F}$.

The current of measuring point A during fault can be expressed as

$$\begin{aligned}\boldsymbol{I}_A &= \boldsymbol{I}_{\rm L} + \boldsymbol{I}_{\rm FA} = \boldsymbol{I}_{\rm L} + \frac{\boldsymbol{Z}_{\rm L2} + \boldsymbol{Z}_{\rm cB}}{\boldsymbol{Z}_{\rm cA} + \boldsymbol{Z}_{\rm LAB} + \boldsymbol{Z}_{\rm cB}} \boldsymbol{I}_{\rm F} \\ &= \boldsymbol{I}_{\rm L} + K \boldsymbol{I}_{\rm F} e^{{\rm j}\gamma}\end{aligned} \tag{19}$$

where $\boldsymbol{I}_{\rm L}$ is the pre-fault current of line AB; $\boldsymbol{I}_{\rm FA}$ is the fault component current of A-side system; $\boldsymbol{Z}_{\rm cA}$ and $\boldsymbol{Z}_{\rm cB}$ are the equivalent impedances of A- and B-side system, respectively; $\boldsymbol{Z}_{\rm L2}$ is the line impedances from B to the fault point respectively; $\boldsymbol{Z}_{\rm LAB} = \boldsymbol{Z}_{\rm L1} + \boldsymbol{Z}_{\rm L2}$; K is the fault component current distribution coefficient of A side; γ is the phase angle between the fault current of A side and the fault current of the transition resistance $R_{\rm F}$.

Based on (18) and (19), the line reactance and resistance from A to the fault point can be described as

$$\begin{cases} X_{\rm L1} = X_A - bR_F / K \\ R_{\rm L1} = R_A - aR_F / K \end{cases} \tag{20}$$

where $a = {\rm Re}(\boldsymbol{I}_{\rm FA}/\boldsymbol{I}_{\rm A} e^{{\rm j}\gamma}), b = {\rm Im}(\boldsymbol{I}_{\rm FA}/\boldsymbol{I}_{\rm A} e^{{\rm j}\gamma}), X_{\rm A}$ and $R_{\rm A}$ are the reactance and resistance measured from A terminal, respectively. In order to eliminate the influence of $R_{\rm F}$, combined line impedance angle, $K/R_{\rm F}$, can be described as

$$K / R_F = (atan\varphi_{\rm L1} - b) / (R_A \tan\varphi_{\rm L1} - X_A) \tag{21}$$

where $\varphi_{\rm L1}$ is the line impedance angle.

Based on (20) and (21), $X_{\rm L1}$ and $R_{\rm L1}$ can be described as

$$\begin{cases} X_{\rm L1} = X_A - (R_A \tan\varphi_{\rm L1} - X_A) / [\tan\varphi_{\rm L1} \cot(\beta - \gamma) - 1] \\ R_{\rm L1} = R_A - (R_A \tan\varphi_{\rm L1} - X_A) / [\tan\varphi_{\rm L1} - \tan(\beta - \gamma)] \end{cases} \tag{22}$$

where $\beta = \arg[(\boldsymbol{I}_{\rm A} - \boldsymbol{I}_{\rm L})/\boldsymbol{I}_{\rm A}]$. Based on Fig. 11 and (21), the fault location information can be deduced as

$$\begin{cases} X_{\rm L} = X_{\rm L1} + X_{\rm cA} \\ R_{\rm L} = R_{\rm L1} + R_{\rm cA} \end{cases} \tag{23}$$

where $X_{\rm cA}$ and $R_{\rm cA}$ are the inductance and resistance between the DFIG and the measurement point, respectively, which are constants. According to the information of the fault location, the rotor active current reference during the grid fault can be calculated by (17). The control block diagram of the optimal current proportion scheme during LVRT is shown in Fig. 13(a). $I_{\rm rM}$ is the maximum current output capacity of the RSC. During the weak grid fault, $I^*_{\rm rq}$ is calculated according to the grid code requirements, and $I^*_{\rm rd}$ should be selected on the basis of the constraint of the RSC maximum current capacity. When the constraint of $I^{*2}_{\rm rd} + I^{*2}_{\rm rq} > I^2_{\rm rM}$ is met, channel 1 will be selected; otherwise, channel 2 will be selected to inject the optimal active current to the power grid.

B. Decreasing PLL Bandwidth Scheme

It can be seen from the analysis of Section III that the small signal stability of the DFIG system can be enhanced by decreasing

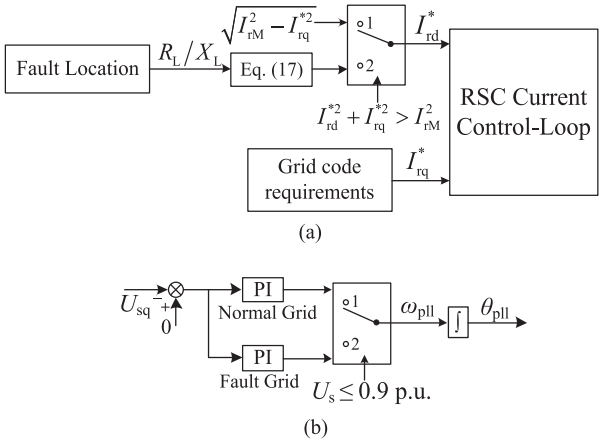

Fig. 13. Control block diagram of the proposed schemes for DFIG-based wind turbine.

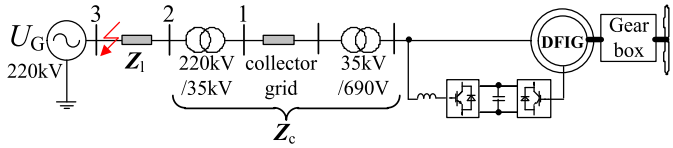

Fig. 14. Aggregated wind power plant and Thevenin equivalent grid for simulation studies.

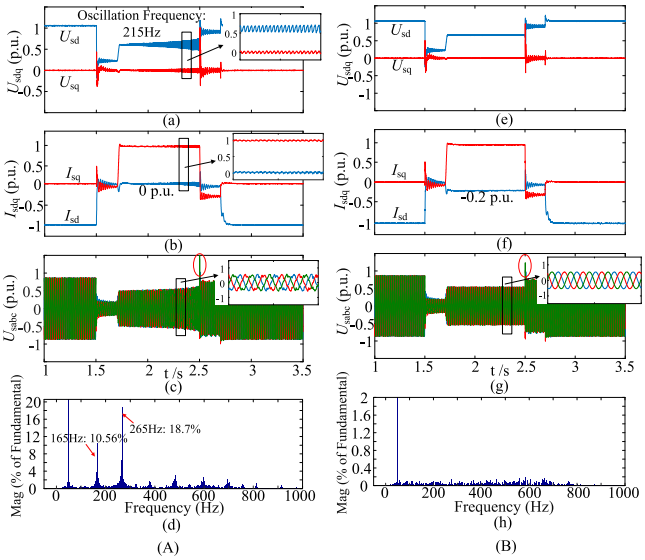

Fig. 15. Simulation results when the grid voltage drops to 0.2 p.u. (A) Adopting traditional LVRT scheme; (B) Adopting optimal current ratio scheme. (a) and (e) Stator dq-axis voltage U_{sd}, U_{sq}; (b) and (f) stator dq-axis current I_{sd}, I_{sq}; (c) and (g) stator three-phase voltage U_{sabc}; (d) and (h) the FFT analysis result of the stator A-phase voltage.

the PLL bandwidth during the grid fault. Moreover, according to Figs. 3, 5, and 10, the dominant eigenvalues are monotonically related to the fault position, the voltage dips degree, and the rotor speed, respectively, i.e., the dominant eigenvalues will move to the left half-plane of the s-plane as the fault position moves toward the PCC and the voltage dips degree and rotor speed reduce. Therefore, it is only necessary to determine the PLL bandwidth of DFIG-based wind turbine running at super-synchronous speed during far-end severe fault of the weak grid, which can guarantee the small signal stability of system during LVRT. Considering the dynamic response of the PLL and the dynamic stability of the DFIG system, the PLL bandwidth during the grid fault is selected to be 11.3 Hz in this paper. This bandwidth can ensure the small signal stability of the system when the fault occurs at different positions and different rotor speeds, which will be also demonstrated by the experimental results in Section V. The control block diagram of decreasing PLL bandwidth scheme is given in Fig. 13(b). Under normal grid condition, the conventional PLL bandwidth of channel 1 will be selected to maintain the normal operating performance of the DFIG system. Otherwise, when the grid fault occurs, i.e., $U_s \leq 0.9$ p.u. [19], the PI controller of channel 2 will be utilized to ensure the dynamic stability of the DFIG system during LVRT.

V. Simulation and Experimental Validations

A. Simulation Validations

In order to verify the correctness of the proposed control schemes, the simulation model is built in MATLAB/Simulink according to the IEEE 3-bus test system in [23], as shown in Fig. 14, in which the synchronous generator at bus 1 is replaced by a DFIG-based wind farm. The wind farm consists of 75×2 MW DFIG-based wind turbines, which are aggregated into a single DFIG [27]. It is connected to the power grid via a step-up transformer and high-voltage cable. The DFIG system parameters are given in Appendix A2.

Fig. 15(A) shows the simulation results of the traditional LVRT control scheme when the grid voltage drops to 0.2 p.u. It can be seen that the DFIG system has oscillation instability during the weak grid severe faults, which is consistent with analysis results. The oscillation frequency in dq frame is 215 Hz, as shown in Fig. 15(a) and (b). Fig. 15(c) shows that the stator three-phase voltage also contains the oscillation components. According to the FFT analysis results, as shown in Fig. 15(d), the stator three-phase voltage contains two oscillation components at 265 and -165 Hz respectively. It indicates that the oscillation components are actually in pairs in stationary frame. The reason is that the oscillation component at the frequency of f in the dq frame is transformed into the stationary frame, which will produce a pair of oscillation components in the stationary frame, i.e., $\pm f + 50$ Hz.

Fig. 15(B) shows the simulation results with the optimal current ratio scheme when the grid voltage drops to 0.2 p.u. Compared with Fig. 15(A), it can be seen that injecting reasonable active current into the grid according to (17) during the fault, i.e., -0.2 p.u., can significantly enhance the dynamic stability of the DFIG system, which proves the correctness of the theoretical analysis and the effectiveness of the optimal current ratio scheme. In addition, comparing Fig. 15(c) and (g) shows that proposed control scheme can also effectively reduce the

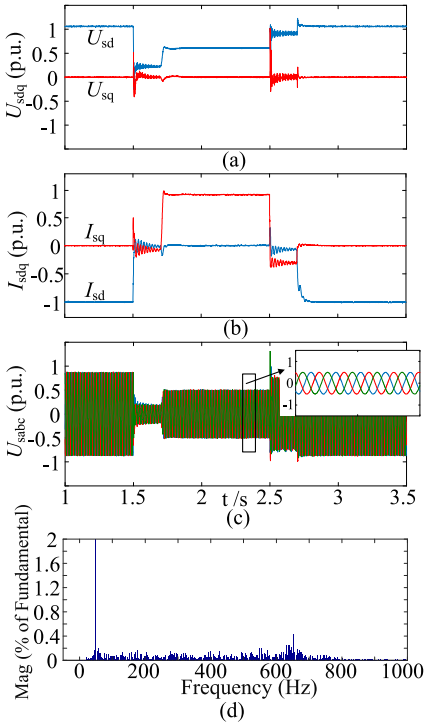

Fig. 16. Simulation results when the PLL bandwidth reduced 11.3 Hz during faults. (a) Stator dq-axis voltage $U_{\rm sd}, U_{\rm sq}$; (b) stator dq-axis current $I_{\rm sd}, I_{\rm sq}$; (c) stator three-phase voltage $U_{\rm sabc}$; (d) the FFT analysis result of the stator A-phase voltage.

transient peak voltage when the grid voltage is restored after the fault. Fig. 15(h) shows the FFT analysis result of the stator A-phase voltage by adopting the proposed optimal current ratio scheme, which indicates that no oscillation will occur during the weak grid fault.

Fig. 16 shows the simulation results with decreasing PLL bandwidth scheme when the grid voltage drops to 0.2 p.u. Compared with Fig. 15(A), when the PLL bandwidth is reduced to 11.3 Hz, the DFIG system can achieve a successful LVRT, which means that the dynamic stability of the DFIG system during fault is enhanced with the decrease of the PLL bandwidth. This confirms the correctness of the theoretical analysis in Section III-D. Fig. 16(d) shows the FFT analysis result of the stator A-phase voltage with the proposed decreasing PLL bandwidth scheme, which also indicates that no oscillation will occur during the weak grid fault when the PLL bandwidth is reduced to a reasonable value.

B. Experimental Validations

In order to further validate the feasibility and effectiveness of the proposed control schemes, the detailed experimental tests were performed on a laboratory-scale DFIG test rig. The schematic diagram and the setup of the experimental system are shown in Fig. 17, and the detailed parameters of the experimental system are given in Appendix A1. As shown in Fig. 17, the DFIG system is driven by a DC motor, and the line impedance is simulated by air-core reactors. The RSC is fed by the Chroma

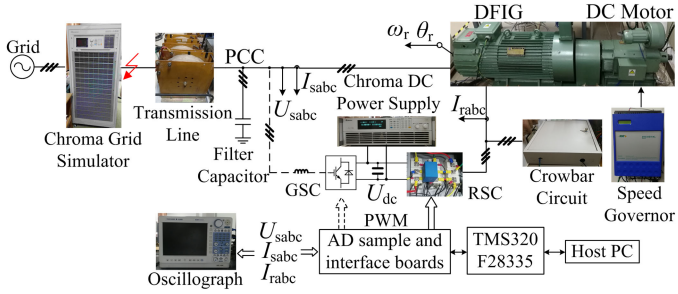

Fig. 17. Schematic diagram of the experimental system.

62150 DC Power Supply and the symmetrical faults of the power grid are generated by using Chroma 61830 Regenerative Grid Simulator.

Fig. 18(A), (B) shows the experimental results that the grid voltage drops to 0.25 and 0.2 p.u., respectively, under the fault condition with $L_{\rm L} = 21$ mH and $R_{\rm L} = 1.5\ \Omega$. The PLL bandwidth is 22.6 Hz, the RCCL bandwidth is 366 Hz, and $\omega_{\rm r} = 0.93$ p.u. Fig. 18(a) and (d) shows the dq components of the stator voltage and rotor current. It can be seen that, with the deepening of the voltage dips degree, the dynamic stability of the DFIG system decreases and the oscillation frequency increases, which is consistent with the analysis in Section III-A. The oscillation frequencies in dq frame are 237 and 247 Hz respectively. Fig. 18(b) and (e) shows that the stator three-phase voltage and stator three-phase current also contain the oscillation components. Fig. 18(c) is the FFT analysis result of the stator A-phase voltage when the voltage drops to 0.25 p.u., which shows that there are two oscillation components at 287 and -187 Hz respectively. Similarly, Fig. 18(f), which is the FFT analysis result of the stator A-phase voltage when the voltage drops to 0.2 p.u., also shows that there are two oscillation components at 297 and -197 Hz respectively.

Fig. 19 shows the experimental results that the grid voltage drops to 0.2 p.u. under the fault condition with $L_{\rm L} = 14$ mH and $R_{\rm L} = 1\ \Omega$. The parameters used in all experiments are the same as in scenario of Fig. 19, except for the paraments specifically stated. Fig. 19(a) shows the dq components of the stator voltage and rotor current. Comparing Figs. 18(d) and 19(a), it is indicated that when the fault position is close to the PCC, the oscillation amplitude decreases and the oscillation frequency increases, which means that the dynamic stability of the DFIG system is enhanced and consistent with the analysis in Section III-B. According to the FFT analysis result of the stator voltage during grid fault in Fig. 19(c), the stator A-phase voltage contains two oscillation components at 301 and -201 Hz respectively, which also proves that the oscillation components in the stationary frame are in pairs. Similarly, the FFT analysis result of the stator A-phase current during grid fault in Fig. 19(d) also shows that the stator current contains two oscillation components at 301 and -201 Hz respectively.

In order to more clearly compare the effect of different rotor speeds on the stability of the DFIG system, the PLL bandwidth is deliberately reduced to 15.6 Hz during grid fault. Fig. 20 shows

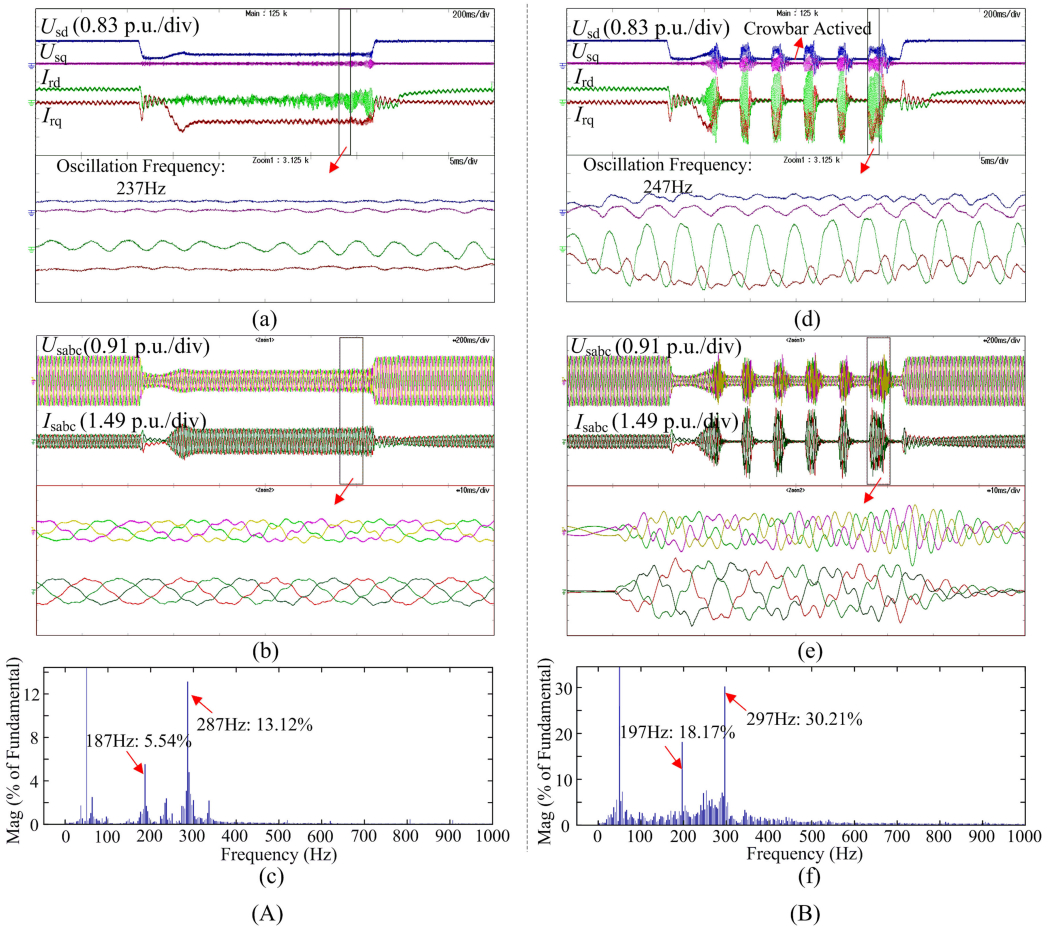

Fig. 18. Experimental results with different voltage dips degree under traditional LVRT control scheme. (A) The grid voltage drops to 0.25 p.u. (B) The grid voltage drops to 0.2 p.u. (a) and (d) Stator dq-axis voltage $U_{\mathrm{sd}}, U_{\mathrm{sq}}$ and rotor dq-axis current $I_{\mathrm{rd}}, I_{\mathrm{rq}}$; (b) and (e) stator three-phase voltage U_{sabc} and stator three-phase current I_{sabc}; (c) and (f) the FFT analysis result of the stator A-phase voltage.

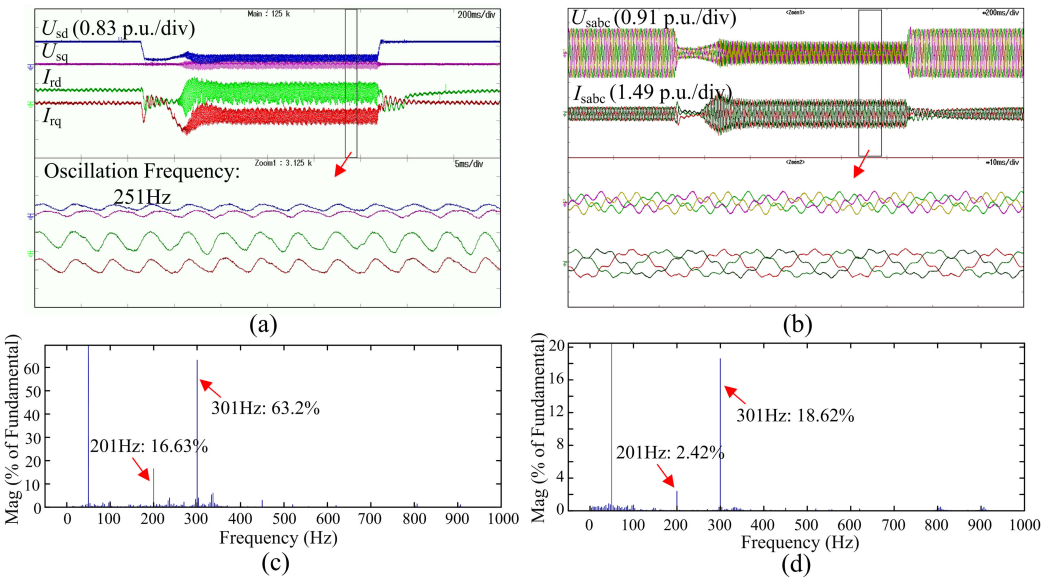

Fig. 19. Experimental results of fault position changes with the traditional LVRT control schemes. (a) Stator dq-axis voltage $U_{\mathrm{sd}}, U_{\mathrm{sq}}$ and rotor dq-axis current $I_{\mathrm{rd}}, I_{\mathrm{rq}}$; (b) stator three-phase voltage U_{sabc} and stator three-phase current I_{sabc}; (c) and (d) the FFT analysis result of the stator A-phase voltage and the stator A-phase current, respectively.

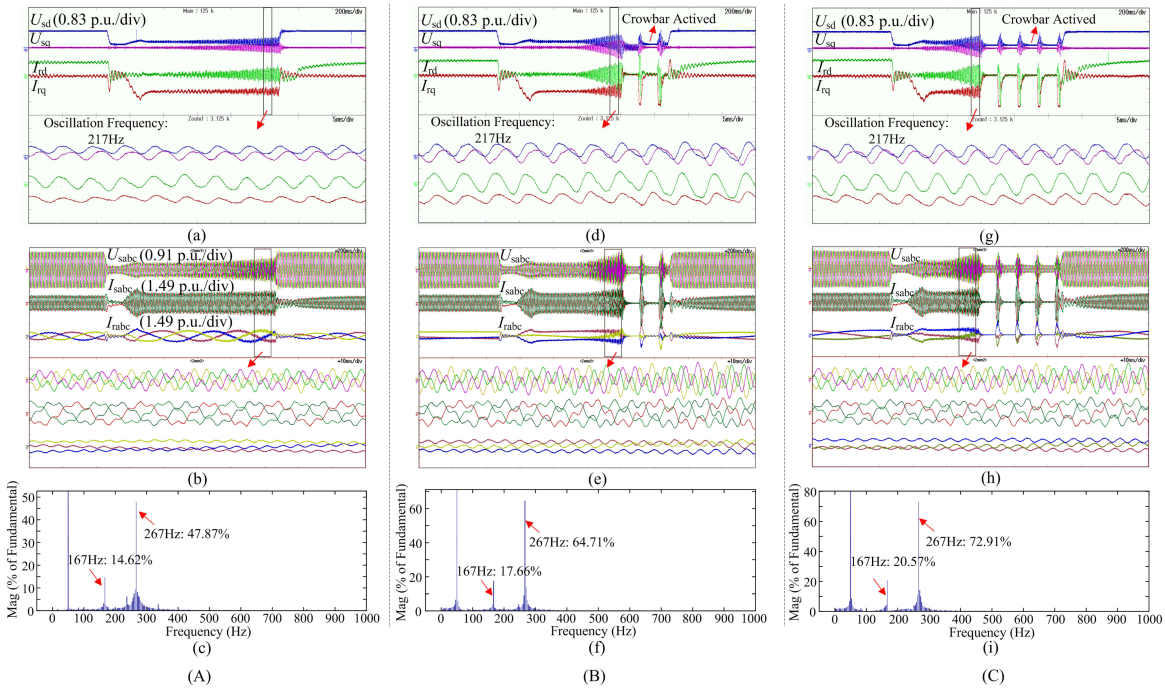

Fig. 20. Experimental results of rotor speed changes with the traditional LVRT control schemes. (A) $\omega_r = 0.93$ p.u. (B) $\omega_r = 1.0$ p.u. (C) $\omega_r = 1.02$ p.u. (a), (d) and (g) Stator dq-axis voltage U_{sd}, U_{sq} and rotor dq-axis current I_{rd}, I_{rq}; (b), (e) and (h) stator three-phase voltage U_{sabc}, stator three-phase current I_{sabc}, and rotor three-phase current I_{rabc}; (c), (f) and (i) the FFT analysis result of the stator A-phase voltage.

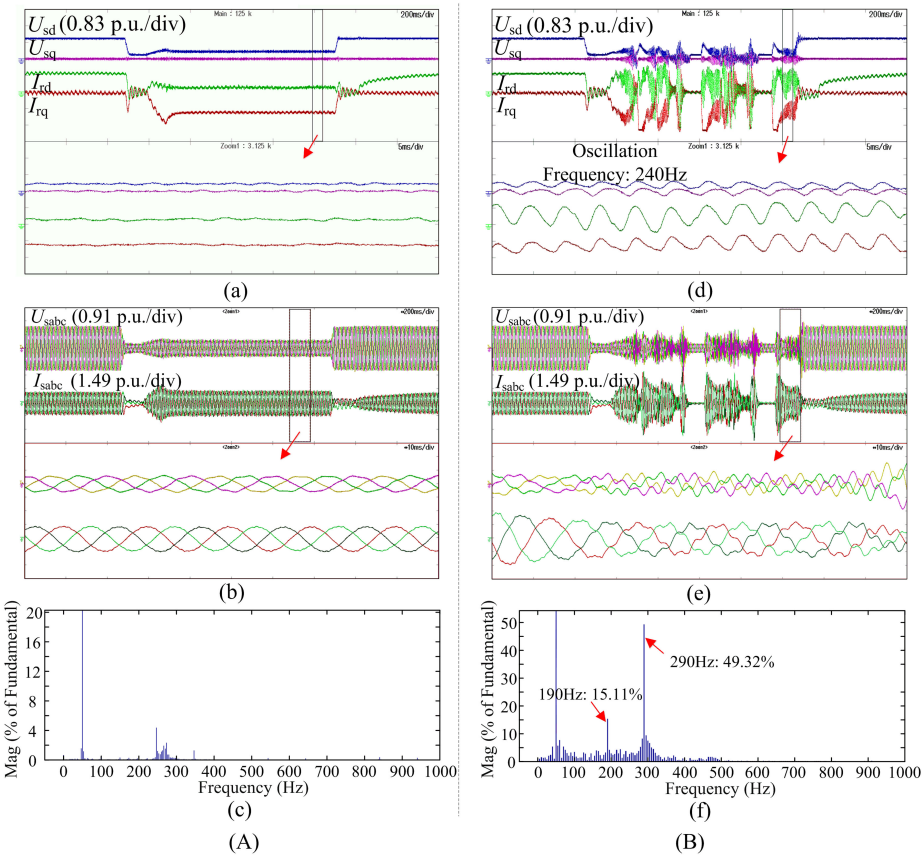

Fig. 21. Experimental results with active current injection during the fault. (A) Injected active current according to the proposed scheme. (B) Injected active current increases to 0.45 p.u. (a) and (d) Stator dq-axis voltage U_{sd}, U_{sq} and rotor dq-axis current I_{rd}, I_{rq}; (b) and (e) stator three-phase voltage U_{sabc} and stator three-phase current I_{sabc}; (c) and (f) the FFT analysis result of the stator A-phase voltage.

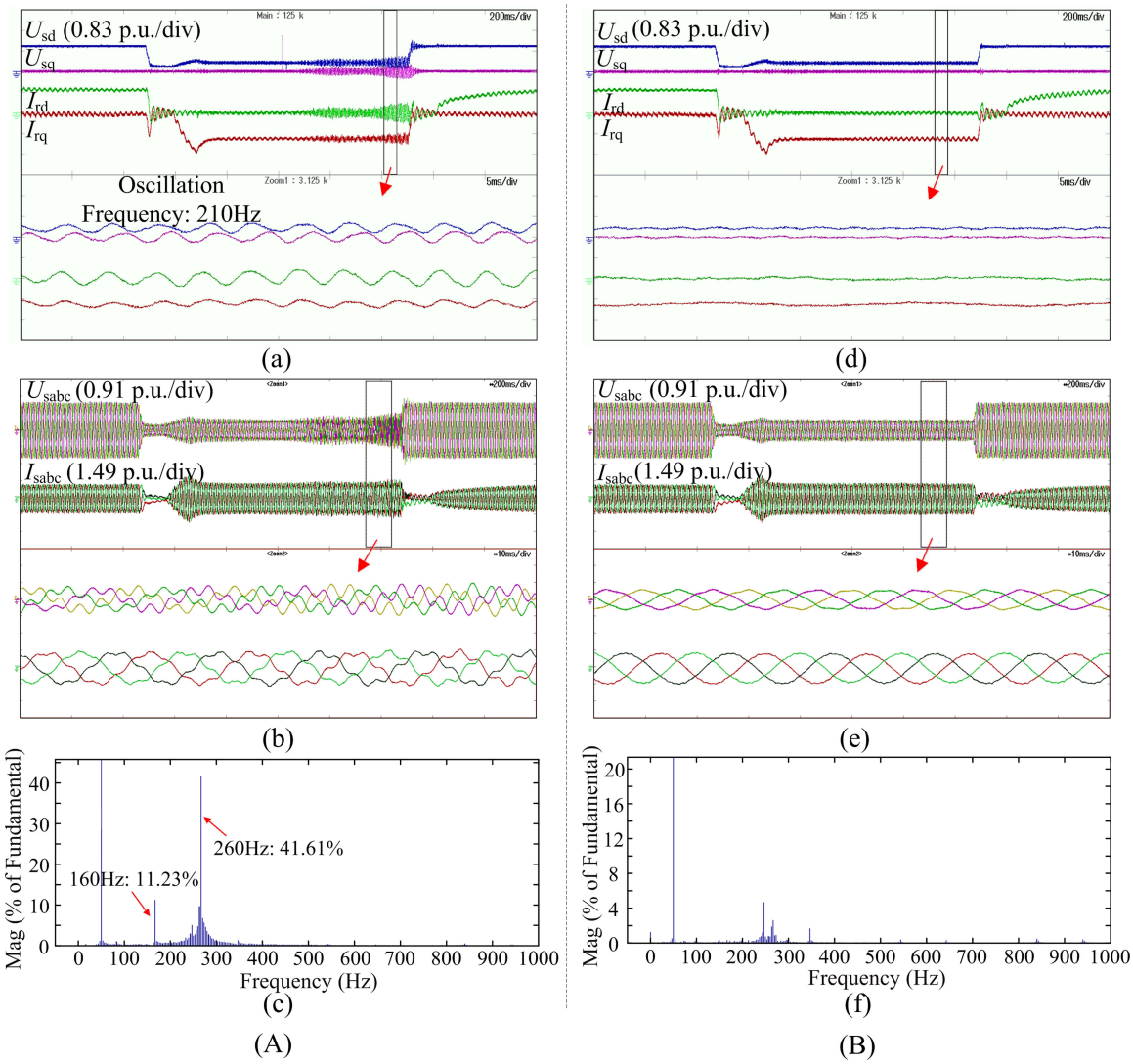

Fig. 22. Experimental results with decreasing PLL bandwidth during the fault. (A) PLL bandwidth decreased to 12.9 Hz. (B) PLL bandwidth decreased to 11.3 Hz. (a) and (d) Stator dq-axis voltage $U_{\rm sd}$, $U_{\rm sq}$ and rotor dq-axis current $I_{\rm rd}$ $I_{\rm rq}$; (b) and (e) stator three-phase voltage $U_{\rm sabc}$ and stator three-phase current $I_{\rm sabc}$; (c) and (f) the FFT analysis result of the stator A-phase voltage.

the experimental results at different rotor speeds when the grid voltage drops to 0.2 p.u. with $L_{\rm L} = 21$ mH and $R_{\rm L} = 1.5\,\Omega$. Comparing Fig. 20(A), (B), and (C), it can be seen that with the increase of the rotor speed, the oscillation amplitude also increases and the dynamic stability of the DFIG system deteriorates during grid fault. Fig. 20(c), (f), and (i) shows the FFT analysis results of the stator A-phase voltage during LVRT, which indicates that the oscillation frequency of the system is basically unchanged under different rotor speeds and consistent with the analysis in Section III-E. In addition, comparing Fig. 18(B) with Fig. 20(A), as the PLL bandwidth decreases, the oscillation amplitude and frequency of the system also decrease, indicating that reducing the PLL bandwidth during the fault is beneficial to the dynamic stability of the system and consistent with the analysis in Section III-D.

Fig. 21 shows the experimental results with the active current injection scheme when the grid voltage drops to 0.2 p.u. with $L_{\rm L} = 21$ mH and $R_{\rm L} = 1.5\,\Omega$. The DFIG-based wind turbine operates at super-synchronous speed. From Fig. 21(A), it can be seen that injecting active current according to (17) can significantly improve the stability of the DFIG system during the grid fault. From Fig. 21(c), the FFT analysis result of the stator A-phase voltage also shows that no oscillation will occur during the weak grid fault. However, if the injected active current increases to 0.45 p.u. during LVRT, as shown in Fig. 21(B), the DFIG system will be unstable again and the oscillation frequency is about 240 Hz, which is consistent with the analysis in Section III-C. Fig. 21(f) shows the FFT analysis result of the stator A-phase voltage during weak grid fault, which indicates that the stator voltage contains a pair of oscillation components at 290 and -190 Hz respectively.

Fig. 22 shows the experimental results with decreasing PLL bandwidth scheme when the grid voltage drops to 0.2 p.u. with $L_{\rm L} = 21$ mH and $R_{\rm L} = 1.5\,\Omega$. The DFIG-based wind turbine

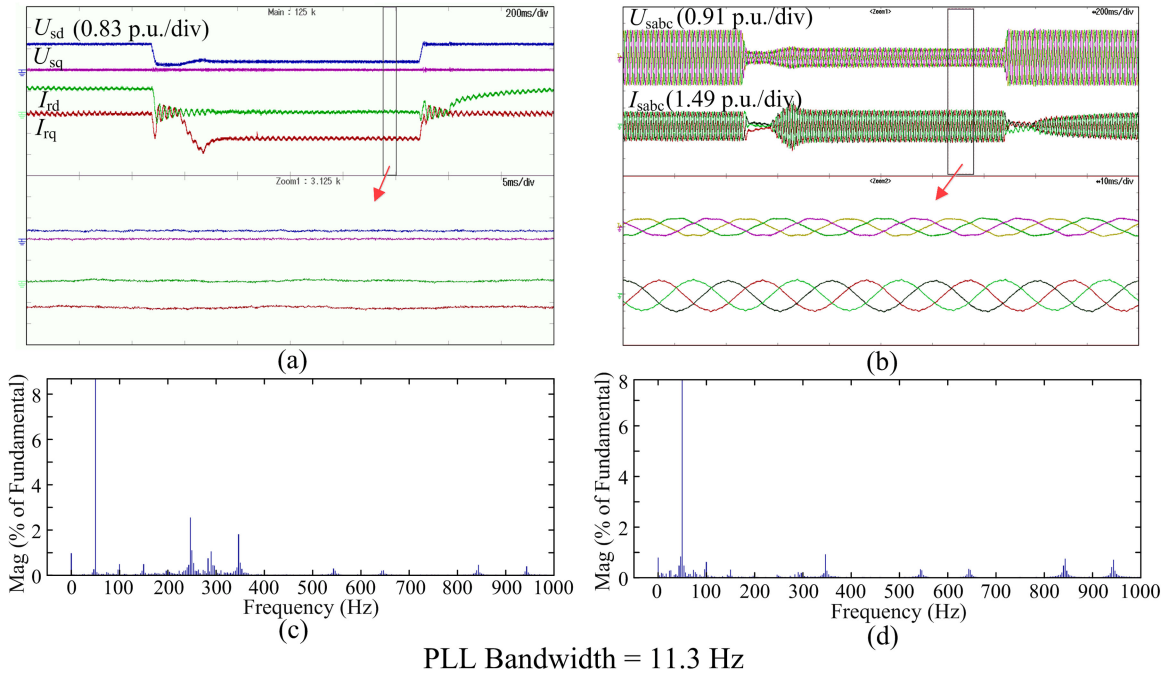

Fig. 23. Experimental results with decreasing PLL bandwidth when the fault position changed. (a) Stator dq-axis voltage $U_{\rm sd}, U_{\rm sq}$ and rotor dq-axis current $I_{\rm rd}, I_{\rm rq}$; (b) stator three-phase voltage $U_{\rm sabc}$ and stator three-phase current $I_{\rm sabc}$; (c) and (d) the FFT analysis result of the stator A-phase voltage and the stator A-phase current, respectively.

operates at super-synchronous speed. Comparing Fig. 20(C) and Fig. 22(A), the small signal stability of the DFIG system is enhanced and the oscillation frequency is also reduced with the decrease of the PLL bandwidth, which verifies the correctness of the theoretical analysis in Section III-D. When the PLL bandwidth is reduced to 12.9 Hz, the DFIG system still oscillates, but the oscillation amplitude is significantly reduced and the oscillation frequency decreases to 210 Hz, as shown in Fig. 22(a). According to the FFT analysis result of the stator A-phase voltage during weak grid fault in Fig. 22(c), there are oscillation components at 260 and -160 Hz respectively. When the PLL bandwidth is reduced to 11.3 Hz, the DFIG system achieves a successful LVRT, as shown in Fig. 22(d), (e). From Fig. 22(f), the FFT analysis result also indicates that no oscillation will occur during the weak grid fault when the PLL bandwidth is reduced to 11.3 Hz.

In order to verify that the PLL bandwidth of 11.3 Hz can guarantee the small signal stability of the DFIG system when the fault occurs at different positions, the experiment under the fault condition with $L_{\rm L} = 14\,{\rm mH}$ and $R_{\rm L} = 1\,\Omega$ has been carried out as shown in Fig. 23. It can be seen from Fig. 23 that, even though the fault position is changing, the DFIG system can realize a successful LVRT, which also validates the correctness of the analysis in Section I'V-B and the practicability of the decreasing PLL bandwidth scheme. Fig. 23(c) and (d) shows the FFT analysis result of the stator A-phase voltage and the stator A-phase current. It also shows that no oscillation will occur during the weak grid fault when adopting the decreasing PLL bandwidth scheme.

VI. Conclusion

The small signal instability that occurs in the DFIG system during the weak grid faults has been verified by the theoretical analysis and experimental tests in this paper. The deeper the voltage dips degree and the higher the rotor speed, the easier the small signal instability of the DFIG system. Moreover, this paper points out that decreasing the PLL bandwidth, increasing RCCL bandwidth, and properly injecting active current into the grid can effectively improve the small signal stability of the DFIG system. Furthermore, it is explained from the mechanism that the instability risk of the system can be minimized when $I_{\rm Gq}/I_{\rm Gd} = -X_{\rm L}/R_{\rm L}$ during the fault. Then, the optimal active current compensation during the grid fault is deduced, which can significantly improve the dynamic stability of the system. Based on the theoretical analysis, two improved LVRT control strategies are proposed in this paper, i.e., the optimal current proportion scheme and the PLL bandwidth selection method. The detailed simulation and experimental results show that the proposed control schemes can effectively improve the small signal stability of the DFIG system during the weak grid severe fault.

In addition, it is worth noting that the DFIG system may also have small signal stability issues during asymmetric fault. Compared with the symmetrical fault of weak grid, the dynamic stability of the DFIG system during unsymmetrical fault is more complicated. When the weak grid asymmetric fault occurs, due to the influence of the long transmission line, the sequence impedances of the system are no longer independent. The coupling of sequence impedance makes the

dynamic stability analysis method and instability mechanism of the DFIG system during weak grid unsymmetrical fault completely different from that during the symmetrical fault. Therefore, the DFIG system dynamic stability during severe unsymmetrical fault of weak grid will be the key point of our next study.

APPENDIX

TABLE A1
EXPERIMENTAL SYSTEM PARAMETERS

Description	Values	Description	Values
Rated Power	3 kW	Pole pairs	2
Rated voltage	220 V	Winding connection	Y/Y
DC-link voltage	400 V	R_s, L_s	0.0068 p.u. 1.285 p.u.
R_r, L_r	0.0961 p.u. 1.346 p.u.	L_m	1.258 p.u.
C_f	0.152 p.u.	R_L, L_L	1.5 Ω, 21 mH
PLL bandwidth	22.6 Hz	RCCL bandwidth	366 Hz

TABLE A2
TIME-DOMAIN SIMULATION SYSTEM PARAMETERS

Description	Values	Description	Values
Rated Power	150 MW	R_s, L_s	0.022 p.u., 0.173 p.u.
Rated voltage	690 V	R_r, L_r	0.026 p.u., 0.167 p.u.
DC-link voltage	1200 V	L_m	2.78 p.u.
PLL bandwidth	17.2 Hz	$\boldsymbol{Z}_l$	0.0646 + j0.2967 p.u.
RCCL bandwidth	247 Hz	$\boldsymbol{Z}_c$	0.0269 + j0.2037 p.u.

B. DERIVATION OF SMALL SIGNAL STATE-SPACE MODEL

The detailed derivation of the small signal state-space model is given in this section. The linearized forms of (3)–(7) at steady-state operation point can be expressed as

$$\begin{cases} \Delta\dot{I}_{\mathrm{sd}} = -\frac{\omega_{\mathrm{b}}R_{\mathrm{s}}}{\sigma L_{\mathrm{s}}}\Delta I_{\mathrm{sd}} + \omega_{\mathrm{b}}\left(\omega_{\mathrm{pll0}} + \frac{L_{\mathrm{m}}^2\omega_{\mathrm{r}}}{\sigma L_{\mathrm{s}}L_{\mathrm{r}}}\right)\Delta I_{\mathrm{sq}} \\ \qquad + \frac{L_{\mathrm{m}}R_{\mathrm{r}}\omega_{\mathrm{b}}}{\sigma L_{\mathrm{s}}L_{\mathrm{r}}}\Delta I_{\mathrm{rd}} + \frac{\omega_{\mathrm{b}}L_{\mathrm{m}}\omega_{\mathrm{r}}}{\sigma L_{\mathrm{s}}}\Delta I_{\mathrm{rq}} + \omega_{\mathrm{b}}I_{\mathrm{sq0}}\Delta\omega_{\mathrm{pll}} \\ \qquad + \frac{\omega_{\mathrm{b}}}{\sigma L_{\mathrm{s}}}\Delta U_{\mathrm{sd}} - \frac{\omega_{\mathrm{b}}L_{\mathrm{m}}}{\sigma L_{\mathrm{s}}L_{\mathrm{r}}}\Delta U_{\mathrm{rd}} \\ \Delta\dot{I}_{\mathrm{sq}} = -\omega_{\mathrm{b}}\left(\omega_{\mathrm{pll0}} + \frac{L_{\mathrm{m}}^2\omega_{\mathrm{r}}}{\sigma L_{\mathrm{s}}L_{\mathrm{r}}}\right)\Delta I_{\mathrm{sd}} \\ \qquad - \frac{\omega_{\mathrm{b}}R_{\mathrm{s}}}{\sigma L_{\mathrm{s}}}\Delta I_{\mathrm{sq}} - \frac{\omega_{\mathrm{b}}L_{\mathrm{m}}\omega_{\mathrm{r}}}{\sigma L_{\mathrm{s}}}\Delta I_{\mathrm{rd}} \\ \qquad + \frac{L_{\mathrm{m}}R_{\mathrm{r}}\omega_{\mathrm{b}}}{\sigma L_{\mathrm{s}}L_{\mathrm{r}}}\Delta I_{\mathrm{rq}} - \omega_{\mathrm{b}}I_{\mathrm{sd0}}\Delta\omega_{\mathrm{pll}} \\ \qquad + \frac{\omega_{\mathrm{b}}}{\sigma L_{\mathrm{s}}}\Delta U_{\mathrm{sq}} - \frac{\omega_{\mathrm{b}}L_{\mathrm{m}}}{\sigma L_{\mathrm{s}}L_{\mathrm{r}}}\Delta U_{\mathrm{rq}} \end{cases} \tag{B1}$$

$$\begin{cases} \Delta\dot{I}_{\mathrm{rd}} = \frac{\omega_{\mathrm{b}}L_{\mathrm{m}}R_{\mathrm{s}}}{\sigma L_{\mathrm{s}}L_{\mathrm{r}}}\Delta I_{\mathrm{sd}} - \frac{\omega_{\mathrm{b}}L_{\mathrm{m}}\omega_{\mathrm{r}}}{\sigma L_{\mathrm{r}}}\Delta I_{\mathrm{sq}} - \frac{R_{\mathrm{r}}\omega_{\mathrm{b}}}{\sigma L_{\mathrm{r}}}\Delta I_{\mathrm{rd}} \\ \qquad + \omega_{\mathrm{b}}(\omega_{\mathrm{pll0}} - \frac{\omega_{\mathrm{r}}}{\sigma})\Delta I_{\mathrm{rq}} + \omega_{\mathrm{b}}I_{\mathrm{rq0}}\Delta\omega_{\mathrm{pll}} \\ \qquad - \frac{\omega_{\mathrm{b}}L_{\mathrm{m}}}{\sigma L_{\mathrm{s}}L_{\mathrm{r}}}\Delta U_{\mathrm{sd}} + \frac{\omega_{\mathrm{b}}}{\sigma L_{\mathrm{r}}}\Delta U_{\mathrm{rd}} \\ \Delta\dot{I}_{\mathrm{rq}} = \frac{\omega_{\mathrm{b}}L_{\mathrm{m}}\omega_{\mathrm{r}}}{\sigma L_{\mathrm{r}}}\Delta I_{\mathrm{sd}} + \frac{\omega_{\mathrm{b}}L_{\mathrm{m}}R_{\mathrm{s}}}{\sigma L_{\mathrm{s}}L_{\mathrm{r}}}\Delta I_{\mathrm{sq}} - \omega_{\mathrm{b}}(\omega_{\mathrm{pll0}} - \frac{\omega_{\mathrm{r}}}{\sigma})\Delta I_{\mathrm{rd}} \\ \qquad - \frac{R_{\mathrm{r}}\omega_{\mathrm{b}}}{\sigma L_{\mathrm{r}}}\Delta I_{\mathrm{rq}} - \omega_{\mathrm{b}}I_{\mathrm{rd0}}\Delta\omega_{\mathrm{pll}} - \frac{\omega_{\mathrm{b}}L_{\mathrm{m}}}{\sigma L_{\mathrm{s}}L_{\mathrm{r}}}\Delta U_{\mathrm{sq}} \\ \qquad + \frac{\omega_{\mathrm{b}}}{\sigma L_{\mathrm{r}}}\Delta U_{\mathrm{rq}} \end{cases} \tag{B2}$$

$$\begin{cases} \Delta\dot{x}_1 = \Delta U_{\mathrm{sq}} \\ \Delta\omega_{\mathrm{pll}} = k_{\mathrm{p1}}\Delta U_{\mathrm{sq}} + k_{\mathrm{i1}}\Delta x_1 \\ \Delta\dot{\theta}_{\mathrm{pll}} = \omega_{\mathrm{b}}\Delta\omega_{\mathrm{pll}} \end{cases} \tag{B3}$$

$$\begin{cases} \Delta\dot{x}_2 = -\Delta I_{\mathrm{rd}} \\ \Delta U_{\mathrm{rd}} = (R_{\mathrm{r}} - k_{\mathrm{p2}})\Delta I_{\mathrm{rd}} + k_{\mathrm{i2}}\Delta x_2 + (U_{\mathrm{sd0}}L_{\mathrm{m}}/L_{\mathrm{s}} \\ \qquad -\sigma L_{\mathrm{r}}I_{\mathrm{rq0}})\Delta\omega_{\mathrm{pll}} + (\omega_{\mathrm{pll0}} - \omega_{\mathrm{r}})L_{\mathrm{m}}\Delta U_{\mathrm{sd}}/L_{\mathrm{s}} \\ \qquad -(\omega_{\mathrm{pll0}} - \omega_{\mathrm{r}})\sigma L_{\mathrm{r}}\Delta I_{\mathrm{rq}} \\ \Delta\dot{x}_3 = -\Delta I_{\mathrm{rq}} \\ \Delta U_{\mathrm{rq}} = (R_{\mathrm{r}} - k_{\mathrm{p3}})\Delta I_{\mathrm{rq}} + k_{\mathrm{i3}}\Delta x_3 \\ \qquad +(\omega_{\mathrm{pll0}} - \omega_{\mathrm{r}})\sigma L_{\mathrm{r}}\Delta I_{\mathrm{rd}} + \sigma L_{\mathrm{r}}I_{\mathrm{rd0}}\Delta\omega_{\mathrm{pll}} \end{cases} \tag{B4}$$

$$\begin{cases} \Delta\dot{U}_{\mathrm{sd}} = \frac{\omega_{\mathrm{b}}}{C_{\mathrm{f}}}(\Delta I_{\mathrm{Gd}} - \Delta I_{\mathrm{sd}}) + \omega_{\mathrm{b}}\omega_{\mathrm{pll0}}\Delta U_{\mathrm{sq}} + \omega_{\mathrm{b}}U_{\mathrm{sq0}}\Delta\omega_{\mathrm{pll}} \\ \Delta\dot{U}_{\mathrm{sq}} = \frac{\omega_{\mathrm{b}}}{C_{\mathrm{f}}}(\Delta I_{\mathrm{Gq}} - \Delta I_{\mathrm{sq}}) - \omega_{\mathrm{b}}\omega_{\mathrm{pll0}}\Delta U_{\mathrm{sd}} - \omega_{\mathrm{b}}U_{\mathrm{sd0}}\Delta\omega_{\mathrm{pll}} \end{cases} \tag{B5}$$

$$\begin{cases} \Delta\dot{I}_{\mathrm{Gd}} = \frac{\omega_{\mathrm{b}}}{L_{\mathrm{L}}}U_{\mathrm{Gqs0}}\Delta\theta_{\mathrm{pll}} - \frac{\omega_{\mathrm{b}}R_{\mathrm{L}}}{L_{\mathrm{L}}}\Delta I_{\mathrm{Gd}} + \omega_{\mathrm{b}}\omega_{\mathrm{pll0}}\Delta I_{\mathrm{Gq}} \\ \qquad -\frac{\omega_{\mathrm{b}}}{L_{\mathrm{L}}}\Delta U_{\mathrm{sd}} + \omega_{\mathrm{b}}I_{\mathrm{Gq0}}\Delta\omega_{\mathrm{pll}} \\ \Delta\dot{I}_{\mathrm{Gq}} = -\frac{\omega_{\mathrm{b}}}{L_{\mathrm{L}}}U_{\mathrm{Gds0}}\Delta\theta_{\mathrm{pll}} - \frac{\omega_{\mathrm{b}}R_{\mathrm{L}}}{L_{\mathrm{L}}}\Delta I_{\mathrm{Gq}} - \omega_{\mathrm{b}}\omega_{\mathrm{pll0}}\Delta I_{\mathrm{Gd}} \\ \qquad -\frac{\omega_{\mathrm{b}}}{L_{\mathrm{L}}}\Delta U_{\mathrm{sq}} - \omega_{\mathrm{b}}I_{\mathrm{Gd0}}\Delta\omega_{\mathrm{pll}}. \end{cases} \tag{B6}$$

Based on (B1)–(B6), the linearized state-space equation of the DFIG-based system is obtained as

$$\begin{cases} \Delta\dot{\boldsymbol{x}} = \boldsymbol{A}\Delta\boldsymbol{x} + \boldsymbol{B}\Delta\boldsymbol{u} \\ 0 = \boldsymbol{C}\Delta\boldsymbol{x} + \boldsymbol{D}\Delta\boldsymbol{u} \end{cases} \tag{B7}$$

where unnoumber equations shown at the top of the next page.

$$
\boldsymbol{A} = \begin{array}{c} \\ 1 \\ 2 \\ 3 \\ 4 \\ 5 \\ 6 \\ 7 \\ 8 \\ 9 \\ 10 \\ 11 \\ 12 \end{array}
\begin{array}{c}
\begin{array}{cccccccccccc} 1 & 2 & 3 & 4 & 5 & 6 & 7 & 8 & 9 & 10 & 11 & 12 \end{array} \\
\begin{bmatrix}
-\frac{\omega_{\mathrm{b}}R_{\mathrm{s}}}{\sigma L_{\mathrm{s}}} & \omega_{\mathrm{b}}(\omega_{\mathrm{pll0}}+\frac{L_{\mathrm{m}}^2\omega_{\mathrm{r}}}{\sigma L_{\mathrm{s}}L_{\mathrm{r}}}) & \frac{L_{\mathrm{m}}R_{\mathrm{r}}\omega_{\mathrm{b}}}{\sigma L_{\mathrm{s}}L_{\mathrm{r}}} & \frac{\omega_{\mathrm{b}}L_{\mathrm{m}}\omega_{\mathrm{r}}}{\sigma L_{\mathrm{s}}} & & & & & \frac{\omega_{\mathrm{b}}}{\sigma L_{\mathrm{s}}} & & & \omega_{\mathrm{b}}I_{\mathrm{sq0}} \\
-\omega_{\mathrm{b}}(\omega_{\mathrm{pll0}}+\frac{L_{\mathrm{m}}^2\omega_{\mathrm{r}}}{\sigma L_{\mathrm{s}}L_{\mathrm{r}}}) & -\frac{\omega_{\mathrm{b}}R_{\mathrm{s}}}{\sigma L_{\mathrm{s}}} & -\frac{\omega_{\mathrm{b}}L_{\mathrm{m}}\omega_{\mathrm{r}}}{\sigma L_{\mathrm{s}}} & \frac{L_{\mathrm{m}}R_{\mathrm{r}}\omega_{\mathrm{b}}}{\sigma L_{\mathrm{s}}L_{\mathrm{r}}} & & & & & & \frac{\omega_{\mathrm{b}}}{\sigma L_{\mathrm{s}}} & & -\omega_{\mathrm{b}}I_{\mathrm{sd0}} \\
\frac{\omega_{\mathrm{b}}L_{\mathrm{m}}R_{\mathrm{s}}}{\sigma L_{\mathrm{s}}L_{\mathrm{r}}} & -\frac{\omega_{\mathrm{b}}L_{\mathrm{m}}\omega_{\mathrm{r}}}{\sigma L_{\mathrm{r}}} & -\frac{R_{\mathrm{r}}\omega_{\mathrm{b}}}{\sigma L_{\mathrm{r}}} & \omega_{\mathrm{b}}(\omega_{\mathrm{pll0}}-\frac{\omega_{\mathrm{r}}}{\sigma}) & & & & & -\frac{\omega_{\mathrm{b}}L_{\mathrm{m}}}{\sigma L_{\mathrm{s}}L_{\mathrm{r}}} & & & \omega_{\mathrm{b}}I_{\mathrm{rq0}} \\
\frac{\omega_{\mathrm{b}}L_{\mathrm{m}}\omega_{\mathrm{r}}}{\sigma L_{\mathrm{r}}} & \frac{\omega_{\mathrm{b}}L_{\mathrm{m}}R_{\mathrm{s}}}{\sigma L_{\mathrm{s}}L_{\mathrm{r}}} & -\omega_{\mathrm{b}}(\omega_{\mathrm{pll0}}-\frac{\omega_{\mathrm{r}}}{\sigma}) & -\frac{R_{\mathrm{r}}\omega_{\mathrm{b}}}{\sigma L_{\mathrm{r}}} & & & & & & -\frac{\omega_{\mathrm{b}}L_{\mathrm{m}}}{\sigma L_{\mathrm{s}}L_{\mathrm{r}}} & & \\
 & & -1 & & & & & & & & & \\
 & & & -1 & & & & & & & & \\
 & & & & & & -\frac{\omega_{\mathrm{b}}R_{\mathrm{L}}}{L_{\mathrm{L}}} & \omega_{\mathrm{b}}\omega_{pll0} & -\frac{\omega_{\mathrm{b}}}{L_{\mathrm{L}}} & & & \frac{\omega_{\mathrm{b}}}{L_{\mathrm{L}}}U_{\mathrm{Gqs0}} \\
 & & & & & & -\omega_{\mathrm{b}}\omega_{\mathrm{pll0}} & -\frac{\omega_{\mathrm{b}}R_{L}}{L_{\mathrm{L}}} & & & -\frac{\omega_{\mathrm{b}}}{L_{\mathrm{L}}} & -\frac{\omega_{\mathrm{b}}}{L_{\mathrm{L}}}U_{\mathrm{Gds0}} \\
-\frac{\omega_{\mathrm{b}}}{C_{\mathrm{f}}} & & & & & & \frac{\omega_{\mathrm{b}}}{C_{\mathrm{f}}} & & & \omega_{\mathrm{b}}\omega_{pll0} & & \\
 & -\frac{\omega_{\mathrm{b}}}{C_{\mathrm{f}}} & & & & & & \frac{\omega_{\mathrm{b}}}{C_{\mathrm{f}}} & -\omega_{\mathrm{b}}\omega_{\mathrm{pll0}} & & & \\
 & & & & & & & & & 1 & & \\
 & & & & & & & & & & & \\
 & & & & & & & & & & &
\end{bmatrix}
\end{array}
$$

$$
\boldsymbol{B} = \begin{array}{c} \\ 1 \\ 2 \\ 3 \end{array}
\begin{array}{c}
\begin{array}{cccccccccccc} 1 & 2 & 3 & 4 & 5 & 6 & 7 & 8 & 9 & 10 & 11 & 12 \end{array} \\
\begin{bmatrix}
-\frac{\omega_{\mathrm{b}}L_{\mathrm{m}}}{\sigma L_{\mathrm{s}}L_{\mathrm{r}}} & & \frac{\omega_{\mathrm{b}}}{\sigma L_{\mathrm{r}}} & & & & & & & & & \\
 & -\frac{\omega_{\mathrm{b}}L_{\mathrm{m}}}{\sigma L_{\mathrm{s}}L_{\mathrm{r}}} & & \frac{\omega_{\mathrm{b}}}{\sigma L_{\mathrm{r}}} & & & & & & & & \\
\omega_{\mathrm{b}}I_{\mathrm{sq0}} & -\omega_{\mathrm{b}}I_{\mathrm{sd0}} & \omega_{\mathrm{b}}I_{\mathrm{rq0}} & -\omega_{\mathrm{b}}I_{rd0} & & \omega_{\mathrm{b}}I_{\mathrm{Gq0}} & -\omega_{\mathrm{b}}I_{\mathrm{Gd0}} & \omega_{\mathrm{b}}U_{\mathrm{sq0}} & -\omega_{\mathrm{b}}U_{\mathrm{sd0}} & & & \omega_{\mathrm{b}}
\end{bmatrix}^T
\end{array}
$$

$$
\boldsymbol{C} = \begin{array}{c} \\ 1 \\ 2 \\ 3 \end{array}
\begin{array}{c}
\begin{array}{cccccccccccc} 1 & 2 & 3 & & & & & 4 & & & & \\ & & & 5 & 6 & 7 & 8 & & 9 & 10 & 11 & 12 \end{array} \\
\begin{bmatrix}
R_{\mathrm{r}}-k_{\mathrm{p2}} & -(\omega_{\mathrm{pll0}}-\omega_{\mathrm{r}})\sigma L_{\mathrm{r}} & k_{\mathrm{i2}} & & & & & \frac{(\omega_{\mathrm{pll0}}-\omega_{\mathrm{r}})L_{\mathrm{m}}}{L_{\mathrm{s}}} & & & & \\
(\omega_{\mathrm{pll0}}-\omega_{\mathrm{r}})\sigma L_{\mathrm{r}} & R_{\mathrm{r}}-k_{\mathrm{p3}} & & & k_{\mathrm{i3}} & & & & & & & \\
 & & & & & & & & & k_{\mathrm{p1}} & k_{\mathrm{i1}} &
\end{bmatrix}
\end{array}
$$

$$
\boldsymbol{D} = \begin{array}{c} \\ 1 \\ 2 \\ 3 \end{array}
\begin{array}{c}
\begin{array}{ccc} 1 & 2 & 3 \end{array} \\
\begin{bmatrix}
-1 & & \frac{U_{\mathrm{sd0}}L_{\mathrm{m}}}{L_{\mathrm{s}}}-\sigma L_{\mathrm{r}}I_{\mathrm{rq0}} \\
 & -1 & \sigma L_{\mathrm{r}}I_{\mathrm{rd0}} \\
 & & -1
\end{bmatrix}
\end{array}.
$$

REFERENCES

[1] K. Ma, L. Tutelea, I. Boldea, D. M. Ionel, and F. Blaabjerg, "Power electronic drives, controls, and electric generators for large wind turbines – an overview," *Elect. Power Compon. Syst.*, vol. 43, no. 12, pp. 1406–1421, Jul. 2015.

[2] A. K. Gupta, K. Verma, and K. R. Niazi, "Dynamic impact analysis of DFIG-based wind turbine generators on low-frequency oscillations in power system," *IET Gener. Transmiss. Distrib.*, vol. 11, no. 18, pp. 4500–4510, Dec. 2017.

[3] H. Liu *et al.*, "Subsynchronous interaction between direct-drive PMSG based wind farms and weak AC networks," *IEEE Trans. Power Syst.*, vol. 32, no. 6, pp. 4708–4720, Nov. 2017.

[4] E. Muljadi, C. P. Butterfield, B. Parsons, and A. Ellis, "Effect of variable speed wind turbine generator on stability of a weak grid," *IEEE Trans. Energy Convers.*, vol. 22, no. 1, pp. 29–36, Mar. 2007.

[5] Y. Yan, J. Hu, Q. Hu, M. Zhao, Y. Li, and H. Tang, "Concerns to the emerging grid codes for wind turbines' LVRT in weak AC grid," in *Proc. IEEE ICEMS*, Oct. 2014, pp. 3036–3040.

[6] C. Wessels, F. Gebhardt, and F. W. Fuchs, "Fault ride-through of a DFIG wind turbine using a dynamic voltage restorer during symmetrical and asymmetrical grid faults," *IEEE Trans. Power Electron.*, vol. 26, no. 3, pp. 807–815, Mar. 2011.

[7] L. G. Meegahapola, T. Littler, and D. Flynn, "Decoupled-DFIG fault ride-through strategy for enhanced stability performance during grid faults," *IEEE Trans. Sustain. Energy*, vol. 1, no. 3, pp. 152–162, Oct. 2010.

[8] Z. Li, R. Li, F. Wang, and Y. Wang, "Study on dynamic LVRT behavior of DFIG considering the influence of the grid," in *Proc. POWERCON*, Oct. 2012, pp. 1–5.

[9] X. Tian, H. Tang, Y. Li, Y. Chi, and Y. Su, "Dynamic stability of weak grid connection of large-scale DFIG based on wind turbines," *J. Eng.*, vol. 2017, no. 13, pp. 1092–1097, 2017.

[10] Y. Song and F. Blaabjerg, "Analysis of middle frequency resonance in DFIG system considering phase-locked loop," *IEEE Trans. Power Electron.*, vol. 33, no. 1, pp. 343–356, Jan. 2018.

[11] Z. Wang, C. Shen, and F. Liu, "Impact of DFIG with phase lock loop dynamics on power systems small signal stability," in *Proc. IEEE PES General Meeting*, 2014, pp. 1–5.

[12] X. Xi, H. Geng, and G. Yang, "Enhanced model of the doubly fed induction generator-based wind farm for small-signal stability studies of weak power system," *IET Renew. Power Gener.*, vol. 8, no. 7, pp. 765–774, Sep. 2014.

[13] J. Hu, Y. Huang, D. Wang, H. Yuan, and X. Yuan, "Modeling of grid-connected DFIG-based wind turbines for DC-link voltage stability analysis," *IEEE Trans. Sustain. Energy*, vol. 6, no. 4, pp. 1325–1336, Oct. 2015.

[14] S. Abulanwar, Z. Chen, and F. Iov, "Enhanced LVRT control strategy of DFIG-based WECS in weak grid," in *Proc. ICRERA*, 2013, pp. 476–481.
[15] C. Ye, J. Ying, J. Hu, Y. Wang, and N. Wang, "Rotor dynamics of DFIG wind turbines under grid faults," in *Proc. ICRPG*, 2015, pp. 1–5.
[16] Y. M. Alsmadi *et al.*, "Detailed investigation and performance improvement of the dynamic behavior of grid-connected DFIG-based wind turbines under LVRT conditions," *IEEE Trans. Ind. Appl.*, vol. 54, no. 5, pp. 4795–4812, Sep./Oct. 2018.
[17] J. Hu, B. Wang, W. Wang, H. Tang, Y. Chi, and Q. Hu, "Small signal dynamics of DFIG-based wind turbines during riding through symmetrical faults in weak AC grid," *IEEE Trans. Energy Convers.*, vol. 32, no. 2, pp. 720–730, Jun. 2017.
[18] R. Liu, J. Yao, J. Pei, X. Wang, P. Sun, and X. Guo, "Dynamic stability analysis of the weak grid-connected DFIG-based wind turbines under severe symmetrical faults," in *Proc. IEEE POWERCON*, Nov. 2018, pp. 1512–1517.
[19] Technical Rule for Connecting Wind Farm to Power System, Chinese Standard: GB/T 19963-2011. Beijing, China: China Electric Power Press, 2011.
[20] F. K. A. Lima, A. Luna, P. Rodriguez, E. H. Watanable, and F. Blaabjerg, "Simplified modeling of a DFIG for transient studies in wind power applications," *IEEE Trans. Ind. Electron.*, vol. 58, no. 1, pp. 9–20, Jan. 2011.
[21] J. Li, J. Yao, X. Zeng, R. Liu, D. Xu, and C. Wang, "Coordinated control strategy for a hybrid wind farm with DFIG and PMSG under symmetrical grid faults," *Energies*, vol. 10, no. 5, pp. 1–21, May 2017.
[22] S. Wang, J. Hu, and X. Yuan, "Virtual synchronous control for grid-connected DFIG-based wind turbines," *IEEE J. Emerg. Sel. Top. Power Electron.*, vol. 3, no. 4, pp. 932–944, Dec. 2015.
[23] P. Kundur, *Power System Stability and Control*. New York, NY, USA: McGraw-Hill, Inc., 1994, ISBN-13: 978-0-07-035958-1.
[24] L. Cai and I. Erlich, "Doubly fed induction generator controller design for the stable operation in weak grids," *IEEE Trans. Sustain. Energy*, vol. 6, no. 3, pp. 1078–1084, Jul. 2015.
[25] B. Wang, J. Suonan, H. Liu, and G. Song, "Long transmission lines fault location based on parameter identification using one-terminal data," in *Proc. APPEEC*, 2012, pp. 1–4.
[26] K. Ramar and E. E. Ngu, "Generalized impedance-based fault location for distribution systems," *IEEE Trans. Power Del.*, vol. 27, no. 1, pp. 449–451, Jan. 2012.
[27] L.M. Fernández, C.A. García, J.R. Saenz, and F. Jurado, "Equivalent models of wind farms by using aggregated wind turbines and equivalent winds," *Energy Convers. Manage.*, vol. 5, no. 3, pp. 691–704, Mar. 2009.

Ruikuo Liu received the B.Eng. and M.Sc. degrees from Southwest Jiaotong University, Chengdu, China, in 2009 and 2012, respectively, both in electrical engineering. He is currently working toward the Ph.D. degree at the School of Electrical Engineering, Chongqing University, Chongqing, China.

His research interests include electric machines control, control of wind turbine generation systems, and renewable power generation.

Jun Yao (M'12) received the B.Eng., M.Sc., and Ph.D. degrees from Chongqing University, Chongqing, China, in 2001, 2004, and 2007, respectively, all in electrical engineering.

Since 2004, he has been with the School of Electrical Engineering, Chongqing University, where he is currently a Professor. He was a Visiting Researcher with the Department of Energy Technology, Aalborg University, Aalborg, Denmark, from January 2012 to January 2013. He is the author/co-author of more than 80 peer-reviewed technical papers, and holds more than 20 issued/pending patents. His research interests include electric machines control, power electronics conversion and control, and renewable power generation; and his main current research interests are wind energy and power electronics application to the power systems.

Dr. Yao is a member of IEC TC 8/SC 8A/JWG 5.

Xuewei Wang received the B.Eng. degree in electrical engineering and automation from the Harbin University of Science and Technology, Harbin, China, in 2016. She is currently pursuing the M.Sc. degree at the School of Electrical Engineering, Chongqing University.

Her research interests include electric machines control, and control of wind turbine generation systems.

Peng Sun received the B.Eng. degree in electrical engineering and automation from Anhui University, Hefei, China, in 2017. He is currently working toward the Ph.D. degree at the School of Electrical Engineering, Chongqing University, Chongqing, China.

His research interests include electric machines control, modeling and control of wind turbine generation system, and renewable power generation.

Jinxin Pei received the B.Eng. degree in electrical engineering and automation from Henan Polytechnic University, Jiaozuo, China, in 2016. He is currently working toward the Ph.D. degree at the College of Electrical Engineering, Chongqing University, Chongqing, China.

His research interests include electric machines control, modeling and control of wind turbine generation system, and renewable power generation.

Jiabing Hu (S'05–M'10–SM'12) received the B.Eng. and Ph.D. degrees in electrical engineering from the College of Electrical Engineering, Zhejiang University, Hangzhou, China, in 2004 and 2009, respectively.

From April 2010 to August 2011, he was a Postdoctoral Research Associate with Sheffield Siemens Wind Power Research Center and with the Department of Electronic and Electrical Engineering, University of Sheffield, Sheffield, U.K. Since September 2011, he has been a Professor with the School of Electrical and Electronic Engineering, Huazhong University of Science and Technology, Wuhan, China. He is an active expert of IEC SC8A WG1/AHG3, and co-convenor of IEC SC8A JWG5. He is the author/co-author of more than 100 peer-reviewed technical papers and one book, and holds more than 20 issued/pending patents. His current research interests include modeling, analysis, and control of power electronized power systems, and MMC for HVdc applications.

Dr. Hu is currently an Editor for the *IEEE Transactions on Energy Conversion* and an Associate Editor for the *IET Renewable Power Generation*. He is the Fellow of the Institute of Engineering and Technology.